NUMERICAL SIMULATION OF THE BROWNOUT OF A HELICOPTER ROTOR IN HIGE CONDITIONS BY COUPLING A FREE-WAKE METHODOLOGY TO A PARTICLE LAGRANGIAN APPROACH

Antonio Visingardi, CIRA – Centro Italiano Ricerche Aerospaziali, Capua (CE), Italy

Abstract

This work presents numerical simulations of the brownout phenomenon produced by the Bo105 helicopter's rotor in HIGE conditions, at a height equal to one rotor blade radius. A Lagrangian approach is implemented in the CIRA free-wake aerodynamic solver RAMSYS to model both the direct entrainment and the bombardment mechanisms of the brownout. Simulations use silica dust and sand of various granulometry, ranging from 1 to $1000\ \mu m$, and density of $2650\ kg/m^3$. The results indicate that particles of $100\ \mu m$ are easily uplifted, while $1\ \mu m$ particles are never mobilized because the friction velocity produced by the rotor flow is not sufficient to break the high inter-particle forces. A toroidal cloud forms around the rotor, which, however, even in the most severe condition, does not obscure the pilot's visibility. Preliminary results are also shown for the brownout produced by coaxial and side-by-side rotors.

1. NOTATION

Symbols

CT	Thrust coefficient $T/\rho\pi R^2(\Omega R)^2$
d_p	Particle diameter, μm
k	Karman's constant, $(=\ 0.41)$
k_r	Nikuradse equivalent roughness length
m_0	Mass of the impacting particle, kg
m_n	Mass of the ejected n particle $(= m_0)$, kg
m_R	Mass of the rebounded particle $(= m_0 = m_n)$, kg
R	Rotor radius, m
T	Thrust of the rotor, N
$\boldsymbol{u}, \boldsymbol{U}$	Flow velocity, m/s
u_*	Friction velocity, m/s
u_{*t}	Threshold friction velocity, m/s
v_h	Inflow velocity in hover $(\Omega R\sqrt{CT/2})$, m/s
$\mathbf{V}_0$	Impacting particle velocity vector, m/s
$\mathbf{V}_n$	Ejected n-th particle velocity vector, m/s
$\mathbf{V}_p$	Particle velocity vector, m/s
$\mathbf{V}_R$	Rebounded particle velocity vector, m/s
v_r	Radial velocity, m/s
$\mathbf{x}_p$	Particle position vector, m
z	Height from the ground, m/s
α_0	Inclination of the impacting particle velocity vector, deg
ρ	Flow density, kg/m^3
ρ_p	Particle density, kg/m^3
θ_0	Collective pitch, deg
Ω	Rotor speed, $1/s$

Acronyms

CIRA	Centro Italiano Ricerche Aerospaziali
HIGE	Hover In Ground Effect
MIM	Method of IMages
RAMSYS	Rotorcraft Aerodynamic Modelling SYStem

2 INTRODUCTION

Brownout is a complex and hazardous phenomenon that affects rotorcraft during landing, take-off, and near-ground flight operations over dusty or sandy unprepared ground surfaces. An illustrative example is shown in Figure 1.

Figure 1: A helicopter encountering brownout conditions

The combined effects of downwash flow and the proximity of the rotor wake to the ground create a velocity field that, when sufficiently intense, can cause loose sediment particles to begin moving. Depending on the vertical velocities near the ground, the sediment may either fall back to the surface or be lifted and carried away by the external flow. The close proximity of the individual vortices in the wake to the sediment bed is likely responsible for stirring up a significant amount of dust, Ref.[1].

This phenomenon involves multiple scales and encompasses complex events such as ground effects on rotor wake, turbulent bursts, surface wall jets, tip vortices, and their interactions. These aerodynamic interactions, combined with particle interactions, create a complicated multiphase phenomenon. Alongside the vortical wake caused by the rotor, there are unsteady effects from the bluff body beneath the rotor, as well as the dynamics of the particles, which further complicate the physics involved. In near-ground operations, highly unsteady wind velocities are common and significantly influence the behaviour of the particulate clouds that lead to brownout conditions.

Rotorcraft can produce various types of dust clouds that differ in size, concentration, and the speed at which they form. For instance, some helicopters create radially expanding, toroidal-shaped dust clouds with minimal vertical dust entrainment, allowing the pilot to maintain good visibility within the cloud. In contrast, other helicopters generate large, dome-shaped dust clouds that can fully envelop the aircraft, often resulting in significant recirculation of dust through the rotor disk. This recirculation can lead to a vertical bombardment of dust particles back onto the ground at relatively high speeds, which stirs up even more dust through a cascading mechanism. Even when the same rotorcraft performs similar take-off or landing manoeuvres, different brownout conditions can arise depending on the characteristics of the surface sediment, including the type and size of the particles, their compaction, moisture content, and other factors.

The loss of visibility caused by dust clouds during brownout conditions can lead to spatial disorientation for pilots, which is a major cause of accidents related to human factors. This can also hinder the autonomous flight of unmanned rotorcraft if their onboard guidance, navigation, and control (GNC) technology relies on vision.

In both scenarios, brownout poses significant risks, leading to loss of life and damage to aircraft. Indeed, rotorcraft operating in brownout conditions suffer from reduced lifetime of rotor blades, engines, and other components due to the abrasive nature of the dust cloud. This dust can also cause malfunctions of onboard sensors.

There are two common ways to mitigate the adverse effects on rotorcraft operations during brownout. The first one is to use on-board sensors to support the pilot to maintain proper orientation and situational awareness of the surrounding area. The second way is to weaken the effects of the wake system generated by the rotor. This can be obtained by acting on several rotorcraft design factors like the number of blades, blade radius, disk loading, blade root cut-out, blade chord, blade twist, blade geometry, rotor speed, ground proximity, rotor and fuselage configuration, and orientation, etc.

To develop an effective strategy for mitigating brownouts, it is essential to understand the fundamental physical principles that lead to the formation of dust clouds due to rotor downwash in various flight conditions. Significant efforts are being made by multiple research laboratories and universities through full-scale flight tests, scaled laboratory tests, and the development of advanced computational models. These initiatives aim to better understand and predict the physics behind brownout characteristics under different operating scenarios. A collection of references related to the experimental studies on brownouts can be found in Ref.[2].

The full-scale flight-test data play an important role in understanding brownout characteristics, but they are rare and may have problems with data quality and repeatability. Laboratory experiments on scaled rotor models were carried out under controlled conditions using particle image velocimetry Refs.[1], [3]. Ghosh and Ragajopalan, Ref.[2], studied the effects of fuselage shapes on rotor in-ground-effect aerodynamics, which is relevant in understanding the problem of rotorcraft brownout. Ramasamy et al., Ref.[4], conducted a series of laboratory experiments to identify and understand various flow phenomena contributing to tandem rotor downwash and outwash, and also evaluated the scaling effects by comparing the model-scale measurements with full-scale measurements.

Data obtained from laboratory-scale experiments are often better conditioned; however, it can be challenging to relate the scaled-down particles used in these experiments to actual full-scale scenarios. While there are very few full-scale flight tests and experiments, and they may have noisy data and scalability issues, these tests provide valuable insights into understanding the brownout phenomenon and help validate computational models.

Due to the limited number of experimental analyses available, computational modelling has become an essential tool for understanding the physics of brownout and for finding ways to mitigate it by adjusting design parameters and operating conditions. Fully validated models can help identify key design and operational factors that influence the overall intensity of the dust cloud, directing research towards more effective long-term solutions for reducing brownout. These factors may include, but are not limited to, careful selection of rotor disk loading, blade loading, rotor tip speed, the number of blades, blade tip shape, number of rotors, and fuselage shape.

Investigating the brownout problem through numerical methods requires consideration of several key aspects. These include: the aerodynamic flow around a rotor in ground effect, the “carrier phase”; the direct entrainment of sediment particles from the ground, due to the shear stresses produced by the rotor flow to the ground particles; the motion of these particles in the air, their interactions with the ground, and the process of saltation bombardment.

Additionally, developing a model for the brownout cloud is particularly complex due to the need for it to:

a) effectively represent multiple modes of particle uplift and entrainment;
b) contain a sufficient number of dust particles to accurately describe the essential features and characteristics of the brownout cloud;
c) avoid including so many particles that the computations become infeasible.

Furthermore, a prerequisite for modelling brownout is the accurate modelling of the time-dependent rotor flow for a rotorcraft manoeuvring near the ground, which in itself is extremely challenging.

Two approaches are popular in modelling particle entrainment and transport processes.

In the Lagrangian approach, the dynamics and trajectories of the representative dust particles under the influence of the rotor flow are modelled using Newton’s second law of motion. The characteristics of the dust cloud are then derived from the behaviour of these representative particles. Wachspress et al. at Continuum Dynamics, Refs.[5], [6], employed a low-fidelity real-time free wake model, coupled with a dust and debris transport model, that uses analytical methods in a Lagrangian framework. D’Andrea, Ref.[7], used a “brownout simulation tool”, a computational chain based on the aerodynamic solver ADPANEL, an unstructured panel code with a time-stepping non-linear free wake vortex model and constant vorticity contour model, which is coupled to a particle transport model to assess the brownout characteristics under unsteady vortical flows of rotorcraft operating on the ground. Leishman and his research group at the University of Maryland also used the Lagrangian approach for particle tracking during a brownout. They coupled the Lagrangian particle tracking model with the free vortex method, Refs.[8], [9], [10], [11], and RANS equations to model the in-ground effect of the rotor during various rotorcraft manoeuvres. Govindarajan and Leishman, Ref.[12], carried out a study on landing manoeuvres with different rotor placement and configuration using a time-dependent free-vortex wake modelling approach. To model the particle transport, they used particle tracking approach based on solutions to a decoupled form of Basset–Boussinesq–Oseen equations appropriate for particles at low Reynolds number Stokes flow.

One of the disadvantages of the free-wake method is that the flow field predicted is inviscid and needs empirical models to approximate the ground boundary layer. A hybrid approach proposed by Thomas et al., Ref.[13], combined the vortex wake method with the Eulerian method to efficiently model the flow field around the rotor while using a Lagrangian approach to model the particle transport. Additionally, the free vortex method with the Lagrangian approach for particle tracking has a high computational cost when wake discretization or the number of particles is increased. This can result in processing time ranging from hours to days on CPUs. To reduce the computational expense of the Lagrangian approach, several techniques can be applied. As relevant examples, D'Andrea adopted a Multi-Processor (MPI) implementation of the ADPANEL code, Ref.[7], whereas Govindarajan et al. applied a particle clustering method, in which the equation of particle motion is applied to a group or cluster of particles instead of individual particles, Ref.[14]. Syal used a GPU-based parallel computing, Ref.[9].

A novel approach to helicopter brownout was developed by Tan et al., Ref.[15], by coupling a vortex particle method and a discrete element method. The dynamics of individual sand particles including the particle-particle and particle-surface interactions was directly computed, and coupled with the flow field of the rotorcraft through air forces acting on individual sand particles. The authors concluded that compared with Lagrangian dust cloud simulations, the front edge and the height of the dust cloud were predicted better by this novel approach.

In the Eulerian approach, the overall dynamics of the particle distribution in the air are modelled using suitable transport equations. This approach was applied to the brownout problem by Ryerson et al., Ref.[16] and Haehnel et al., Ref.[17]. Both these works use a two-phase model to represent the particle dynamics and assume a one-way coupling between the fluid and the particles, that is, the fluid affects the particle but not the other way around. Another study of the brownout problem using the Eulerian approach was conducted by Phillips and Brown, Refs.[18], [19]. They used the vorticity transport model to solve the rotor flow field and coupled it with an Eulerian-based dust transport equation to represent the dust entrainment process. The dust transport model uses empirical correlations borrowed from sedimentology to model the evolution of particle density distribution and its relation with the flow field velocity and vorticity.

Both the Lagrangian and Eulerian approach have their advantages and disadvantages. On the one hand, the Lagrangian approach can model the dynamics of distribution of the particles with varying properties with great details. Accurate modelling of particle dynamics is particularly important near the ground, where the saltation process with particle upliftment by discrete vortices and bombardment mechanisms occurs. The disadvantage of the Lagrangian approach is that it needs to model a very large number of particles to accurately measure the dust density within the flow around the rotorcraft. On the other hand, in the Eulerian approach, the particles are represented by particle density field. The dynamics of particulate distribution are obtained by solving a partial differential equation (PDE) that governs the evolution of particle density, thus making the process computationally very efficient. The disadvantage is that it cannot model the local particle dynamics such as saltation near the ground and needs some particle flux model to handle the entrainment process.

Rovere et al., Ref.[20], presented a comparison of brownout simulations using both Lagrangian and Eulerian frames of reference. They concluded that, although the results exhibited very similar behaviour in terms of cloud shape and size, the Eulerian model is generally more cost-effective in terms of computational resources.

The present work illustrates the implementation activity, carried out at CIRA, of a Lagrangian approach in the in-house free-wake aerodynamic solver RAMSYS for the numerical simulation of the brownout of a helicopter rotor in HIGE conditions. In particular, section 3 describes the main characteristics of the aerodynamic solver and the results of the carrier phase. The particle transport model, at the base of the brownout direct entrainment mechanism, and the bombardment mechanism are illustrated, along with the results obtained, in sections 4 and 5, respectively. In addition, section 6 shows the results of the brownout produced by the direct entrainment mechanism on a counter-rotating coaxial rotor and by a side-by-side co-rotating and contra-rotating rotor. Finally, section 7 outlines the principal conclusions drawn from this study and delineates possible future developments.

3 THE ROTOR FLOW (THE CARRIER PHASE)

3.1 The numerical solver RAMSYS

The unsteady flow induced by the rotorcraft was modelled by using the in-house developed medium-fidelity code RAMSYS, Ref.[21]. which is an unsteady, inviscid and incompressible free-wake vortex lattice boundary element methodology (BEM) solver for multirotor, multi-body configurations developed at CIRA. It is based on Morino's boundary integral formulation for the solution of Laplace's equation for the velocity potential φ. The surface pressure distributions are evaluated by applying the unsteady version of Bernoulli equation, which is then integrated to provide the forces and moments on the configuration and the surrounding obstacles. A computational acceleration is obtained by applying the module for symmetrical flows and geometries implemented in the solver and the parallel execution via the OpenMP API.

3.2 The Bo105 helicopter

All the brownout simulations described in the present document dealt with the full-scale main rotor of the Bo105 helicopter hovering, in ground effect (HIGE), one blade radius above the ground ($z/R = 1$).

The Bo105 is a small multipurpose helicopter built by MBB (now Airbus Helicopters) and is powered by two Allison 250 C20 engines. It is a relatively small helicopter with an empty weight of about $1200 kg$ and a maximum gross weight of $2300 kg$. Typical uses of the highly manoeuvrable Bo105 helicopter are transport, off-shore, police, and military missions. The Bo105 has a hingeless main rotor with four rectangular blades, constituted by a NACA23012 airfoil, and a two-bladed teetering tail rotor. The main rotor is installed $3\ m$ ($z/R = 0.61$) from the ground. The cabin has a height of $1.25\ m$ and its top is approximately located $1\ m$ below the main rotor. The main properties are summarized in Table 1, while the details can be found in Lehmann, Ref.[22].

Figure 2: Bo105 helicopter

Table 1: Main characteristics of the Bo105 main rotor

Description	Value
Radius, R	$4.912\ m$
Rotor speed, Ω	$424\ RPM$
Blade chord, c	$0.27\ m$
Number of blades	4
Pre-cone angle, β_0	$2.5\,^{\circ}$
Main rotor shaft tilt, α_{sh}	$-3.0\,^{\circ}$
First aerodynamic section ($22\%R$)	$1.1\ m$
Twist (linear), θ_{tw}	$-6.2\,^{\circ}$
Effective blade mass, M	$24.2\ kg$

In order to expedite the calculation, the fuselage and the tail rotor were not included in the calculations. In addition, the pre-cone and the shaft tilt angles were set equal to zero for simplicity.

3.3 Space and time discretization

In consideration of the extremely intensive calculations required for the brownout simulations, the discretization of each of the four rectangular blades was limited to 20 panels chordwise and 10 panels spanwise, with a refinement toward the blade tip in order to have a more accurate description of the tip vortex. Similarly, an azimuth step of $15°$ was used for each rotor revolution. Both the number of wake spirals and rotor revolutions were set equal to 21 in order to enable a $3s$ simulation of the brownout phenomenon.

3.4 Analysis of the Bo105 main rotor in HIGE

The aerodynamics of the Bo105 main rotor hovering in ground effect (HIGE) was simulated by applying the Method of Images (MIM).

The application of this method is accurate and efficient, but it can only be employed when symmetry conditions in the flow field are identifiable. This is not the case for a rotor flying near surfaces of arbitrary shapes, where this method cannot be used. Instead, the Surface Singularity Method (SSM), offering greater modelling flexibility, would be necessary, although more computationally intensive.

However, in consideration of the relevant computational time required for brownout simulations, it was assumed that they would be carried out only for rotorcraft in the proximity to flat surfaces, which can therefore be simulated by a symmetry plane. With this assumption, the ground effect was modelled by applying the MIM only.

The main rotor was trimmed in hover flight out of ground effect (HOGE) in order to produce the thrust required to balance the helicopter weight of $2300\ kg$. This was obtained by setting the blade collective pitch θ_0 to $8.08°$. This value was kept constant in all the calculations in HIGE conditions. In order to evaluate and demonstrate the capability of RAMSYS to simulate HIGE flight conditions, a direct comparison was made with the analytical expression by Cheeseman and Bennett, Ref.[23], of the thrust increase in IGE conditions with respect to the OGE condition.

In hover flight, the analytical expression is given by the relationship:

$$\frac{T_{IGE}}{T_{OGE}} = \frac{1}{1-\left(\frac{R}{4z}\right)^2} \quad (1)$$

which is obtained by considering the power as constant.

Figure 3 illustrates the numerical predictions both at constant collective pitch and at constant power (more precisely, since RAMSYS is an inviscid solver, the results were obtained at constant induced power). As expected, the ones at constant power produced a very satisfactory agreement with the analytical formula.

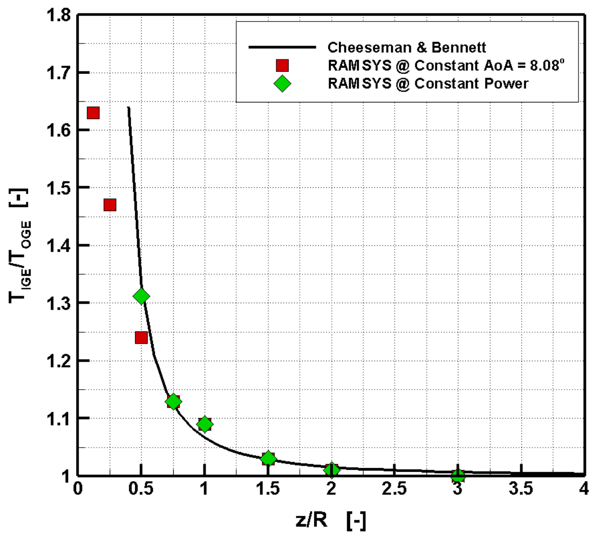

Figure 3: Rotor thrust ratio T_{IGE}/T_{OGE} - Comparison between RAMSYS numerical results and the Cheeseman & Bennet analytical ones.

Figure 4 illustrates the time history of the wake development. As the wake approaches the ground, the initial downwash is deflected in an outwash, pushing the wake roll-up outward all around the ground surface (referred to as groundwash).

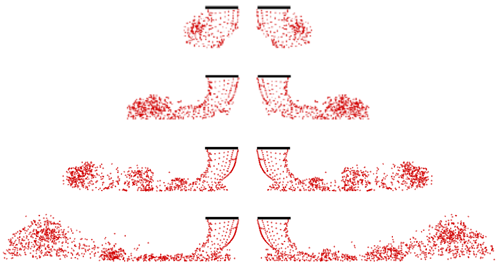

5 Revs.
10 Revs.
15 Revs.
21 Revs.

Figure 4: Time history of the wake development – Cross-sectional planes

The final shape of the wake system, after 21 rotor revolutions, is shown in Figure 5, while Figure 6 highlights the groundwash process and the strong vortex roll-up occurring at the outer boundary of the wake system. These are the two mechanisms that trigger the particle entrainment, which gives rise to the brownout.

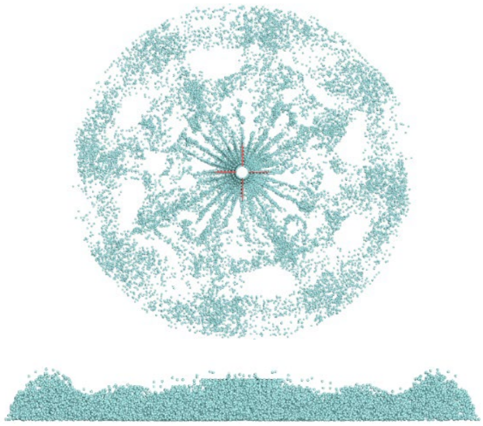

Figure 5: Wake development after 21 rotor revolutions – Top view (top); Side view (bottom)

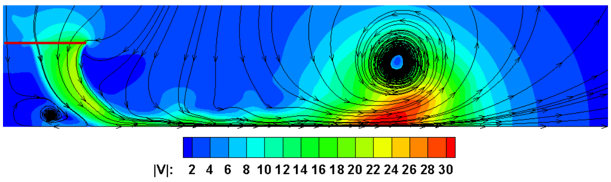

Figure 6: Time-averaged induced velocity contour map & Streamlines after 21 rotor revolutions – Cross-sectional plane passing through the rotor hub centre.

The change with height from the ground of the radial velocities in the wake, generated by the rotor in HIGE condition, is illustrated in Figure 7 for six radial distances from the rotor hub. These velocities were non-dimensionalized with respect to the inflow velocity $v_h = \Omega R\sqrt{CT/2}$. With reference to Figure 6, it can be observed that around the rotor blade tip, the velocity change with height is mainly produced by the shear layer and extends over the whole height. Outside of the rotor, the change in radial velocity is concentrated in the proximity to the ground with a maximum value reached at the radial station $r/R = 1.50$. This is the result of the groundwash that is generated by the presence of the ground, which deflects the rotor downwash outward.

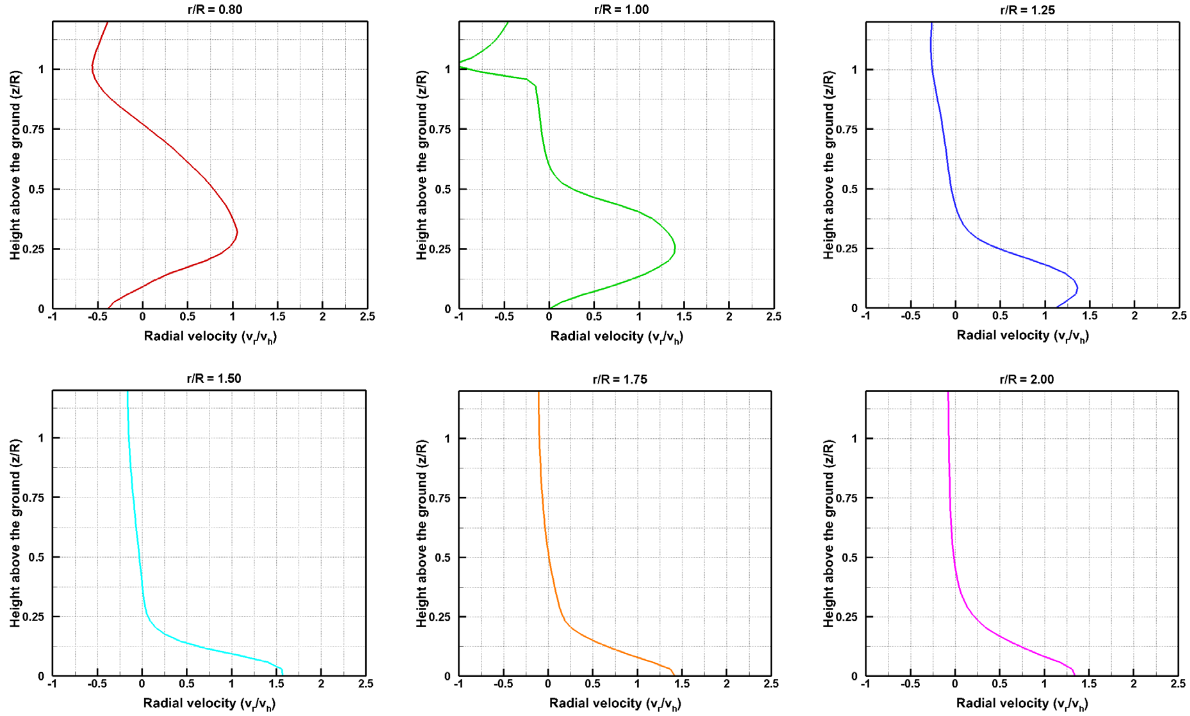

Figure 7: Radial velocities of the rotor in HIGE

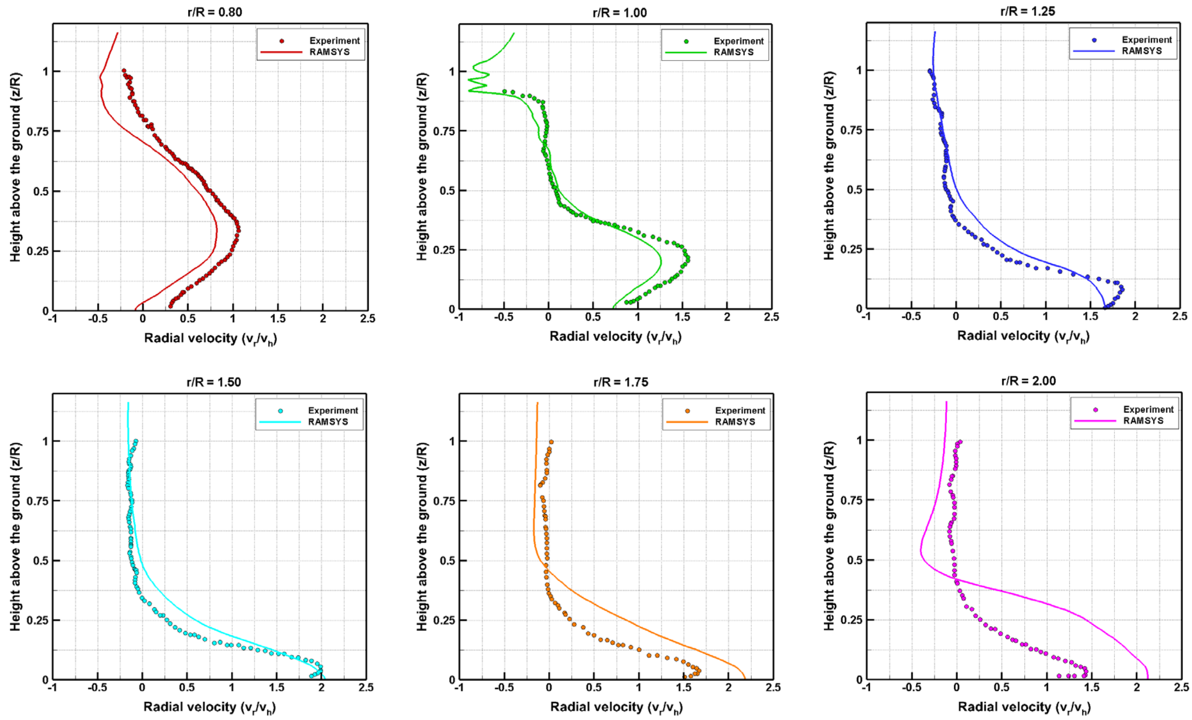

Figure 8: Radial velocities of the rotor in HIGE for the small-scale rotor of Ref.[24]

The lack of flow field experimental data for this configuration did not allow the validation of the predicted radial velocities. For this reason, additional calculations were made for a test case proposed by Lee et al., Ref.[24], for which the experimental radial velocities were available. The rotor is a small one with two blades, in ground effect at $z/R = 1$, having rectangular blades of radius $R = 0.086\ m$, chord $c = 0.019\ m$ and speed $\Omega = 3600\ RPM$. The experimental thrust coefficient CT was set equal to 0.015. Figure 8 shows the comparisons at six radial stations. The agreement with the experimental measurements is satisfactory until the radial station $r/R = 1.50$. Beyond this station, the numerical results show a higher acceleration of the velocity while approaching the ground surface.

4 PARTICLE TRANSPORT MODEL

A brownout particle cloud is composed by billions of sediment particles per cubic volume that span a wide range of diameters. On the Earth, studies conducted by Cowherd on the brownout characteristics generated by six rotorcraft, Ref.[25], demonstrated that the dimension of these particles ranges from $2\ \mu m$ to $350\ \mu m$. Depending on their diameter, they are classified as dust if their diameter is $< 62.5\ \mu m$, and as sand if their diameter is between 62.5 and $2000\ \mu m$. The mechanism through which this particle cloud generates and develops in time is explained in the present section.

4.1 Friction velocity

Particles of dust and sand, initially at rest below the boundary layer flow, are subject to several forces, including inter-particle cohesive, lift, drag, and gravitational forces, as shown in Figure 9.

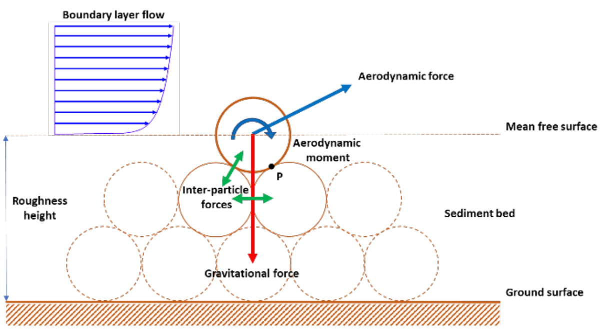

Figure 9: Forces acting on a particle initially at rest on the ground surface

The aerodynamic forces acting on the stationary particle are produced by the surface boundary layer flow, which causes the rise of strong shear stresses τ on the particle to which correspond a friction velocity u_* conventionally expressed as:

$$u_* = \sqrt{\tau/\rho} \qquad (2)$$

Bagnold, Ref.[26], observed that an increase in the velocity induced by the surface flows increases the friction velocity, and where it reaches a certain threshold, i.e., $u_* > u_{*t}$, particles that are initially in equilibrium on the ground then move downstream in saltation under the effect of the lift force, in the absence of impact with other particles. Owen, Ref.[27], evaluated a simple expression for the initial vertical velocity in the saltation layer as expressed by $V_{pz} = 2.8u_{*t}$. This expression was used in the present investigation.

In order to quantify the entity of the friction velocity u_*, the properties of the turbulent boundary layer generated by the surface flow must be known. In the present investigation, centred on an inviscid model of the aerodynamics, the external flow is predicted but the near-wall boundary layer region itself is not resolved. In this case, a self-similar logarithmic velocity profile of the form:

$$u(z) = \frac{u_*}{k} log\left(\frac{z}{k_r}\right) \qquad (3)$$

is assumed in this boundary layer region. The term z is the average height of the particle within the boundary layer, k is the Karman's constant, equal to 0.41, and k_r represents the Nikuradse equivalent roughness length. Its value usually depends on several characteristics of the flow and the surface properties but a common approximation is to use the value $k_r = d_p/30$, which is valid for a flat bed of sand particles.

The process for finding u_* with an inviscid model also requires the assumption of a nominal boundary layer thickness, δ. In this case:

$$u_* = \frac{u(\delta)}{klog(\delta/k_r)} \qquad (4)$$

where $u(\delta)$ is evaluated by the RAMSYS inviscid aerodynamic solver. Experiments have shown that the thickness of the boundary layer in the fully developed wall-jet flow on the ground below a rotor is of the order of 5% of rotor radius, Refs.[1], [24], [28]. This assumption was followed in the present investigation, and a boundary layer thickness $\delta = 0.25m$ was used. Figure 10 illustrates a contour map of the variation of the time-averaged groundwash velocity at the outer edge of the boundary layer δ. In addition, the distribution along the longitudinal and lateral axes is also represented. Underneath the rotor disk, the velocity is extremely small but increases rapidly moving outward and away from the rotor, reaching a maximum value in the region where the wake roll-up occurs.

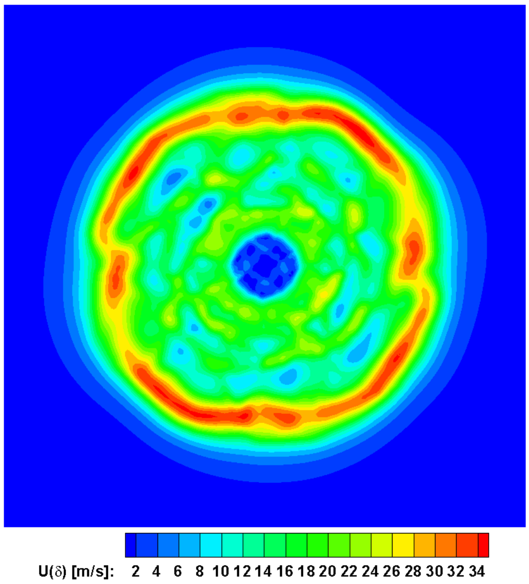

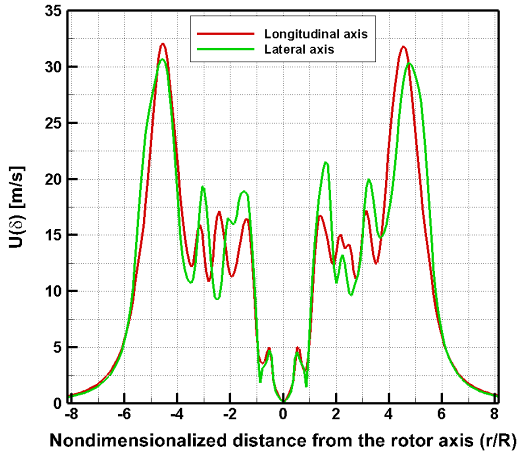

Figure 10: Variation of time-averaged groundwash velocity at the outer edge of the boundary layer – Contour map (left); Distribution along longitudinal and lateral axes (right)

4.2 Threshold friction velocity

Fundamentally, u_{*t} is a measure of the inertia of the surface to the boundary layer shear stress acting on sediment bed and its value is affected by moisture content, roughness, cohesiveness, and other factors.

Bagnold, Ref.[26], derived a threshold friction velocity expression considering the effect of only aerodynamic drag and gravity forces, which can be applied with success to particles of large size only. The major limitation of this model is in the fact it cannot be applied to small particles where cohesive inter-particle forces, including van der Waals forces, water adsorption forces, and electrostatic forces, dominate. Cohesive forces are the most difficult to measure and can only be approximately estimated for the development of mathematical models. Greeley and Iversen, Ref.[29], extended Bagnold's model to the consideration of inter-particle forces, but the resulting expression involves complicated empirical functions. Therefore, a simplified and elegant expression for u_{*t}, found by Shao and Lu, Ref.[30], is commonly used, i.e.:

(5) $$u_{*t} = A\sqrt{\frac{\rho_p - \rho}{\rho} g d_p + \frac{\beta}{\rho d_p}}$$

where $A = 0.1109$ and $\beta = 3 \times 10^{-4}$ for aeolian flows. The first term under the square root corresponds to Bagnold's term, applicable to large particles and linearly increasing with the particle diameter. The second term accounts for the inter-particle cohesive forces which dominate the small particle and is inversely proportional to the particle diameter. Figure 11 shows an example of the variation of the threshold friction velocity with particle size of silica sand. It can be seen that u_{*t} reaches a minimum for particles of intermediate sizes (about $100\ \mu m$). For larger particles, gravitational forces dominate and the friction velocity increases with $\sqrt{d_p}$. For smaller particles, the inter-particle cohesive forces increase the threshold friction velocity and thereby limit particle motion through the mechanism of saltation. Notice that the value of u_{*t} is higher for particles of sizes smaller than $10\ \mu m$. However, the concentrations of particles with sizes $<$ $10\ \mu m$ tend to dominate the developments in a typical brownout dust cloud. This suggests that the direct aerodynamic entrainment after reaching threshold conditions is not the only mechanism with which dust particles are entrained into a brownout cloud. Indeed, another mechanism of the entrainment of dust particles is through the saltation motion of larger particles, which can impact the sediment bed and cause the ejection of new particles through a process known as bombardment.

Finally, Figure 11 also shows the values of the velocities at the edge of the boundary layer beyond which the entrainment process is activated. It is clearly observable that, due to the high inter-particle cohesive forces, much higher velocities are required to entrain small particles than big ones.

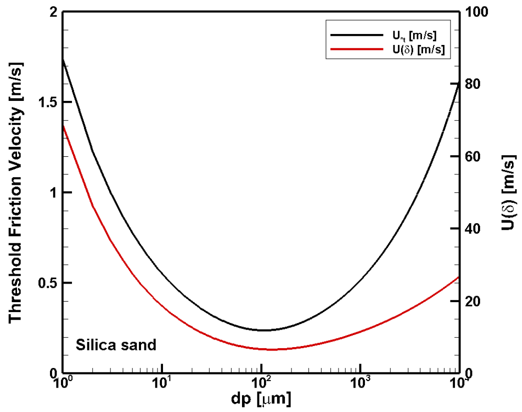

Figure 11: Variation of the threshold friction velocity and of the velocity at the outer edge of the boundary layer as a function of the particle diameter

4.3 Particle convection

Once the particles are entrained into the flow field near the ground, the resulting forces acting on the particles govern their convective motion. It is assumed hereafter that the resulting two-phase flow is lightly loaded by the particles, in that the particle motion is driven by the air but not vice versa (i.e., one-way coupling), which is an approximation strictly valid for low particle densities only. This means that the particles are considered as a discrete phase and the pathway of each individual particle is tracked in time.

In the most general case, the forces acting on the particles include a drag force F_D, a lift force F_L, gravity force F_G, buoyant force F_B, apparent mass forces F_m, Basset forces F_{Basset}, etc. The Basset-Boussinesq-Oseen (BBO) equations govern the resulting dynamic behaviour of the particles. The Bassett force, which depends on the time-history of the particle motion, manifests as an apparent drag force ,but it can be neglected because it is important only in flows with light particles and steep velocity gradients. Furthermore, apart from drag and gravitational forces, all other forces vary proportionally to the ratio of the gas to particle density, which is of the order of 10^{-3} in air. Therefore, perhaps with some exceptions, the other forces can be justifiably neglected for brownout problems.

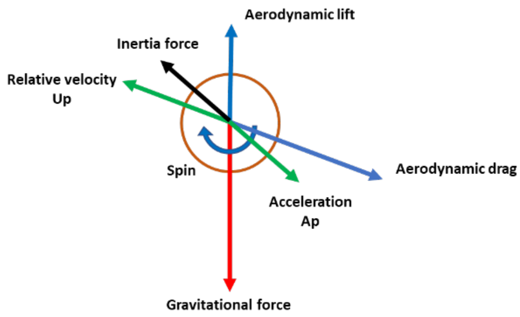

Figure 12: Forces acting on the air-borne particle

Referring to Figure 12, the BBO equations of motion describing the particles can then be simplified to:

$$m\frac{d\boldsymbol{V}_p}{dt} = \sum \boldsymbol{F} \cong \boldsymbol{F}_D + \boldsymbol{F}_G = -\frac{1}{2}\rho C_D A|\boldsymbol{V}_p - \boldsymbol{U}|(\boldsymbol{V}_p - \boldsymbol{U}) + m\boldsymbol{g} \tag{6}$$

where $\boldsymbol{V}_p$ and $\boldsymbol{U}$ are the particle and flow velocity vectors, respectively, at any instant in time.

In the present model, spherical particles with an equivalent diameter of d_p were assumed, so $A = \pi\, d_p^2/4$. The drag coefficient, C_D is a function of particle Reynolds number Re_p, i.e.:

$$C_D(Re_p) = \frac{24}{Re_p}\left(1 + 0.15Re_p^{0.687}\right) \tag{7}$$

where

$$Re_p = \frac{|\boldsymbol{V}_p - \boldsymbol{U}|d_p}{\nu} \tag{8}$$

For the size of particles prominent in brownout clouds then $Re_p \ll 1$, i.e., the particles behave as in Stokes' flow. For such flows, C_D is given by:

$$C_D = \frac{24}{Re_p} \tag{9}$$

Eq. (6) can be rearranged in a more compact form as:

$$\frac{d\boldsymbol{V}_p}{dt} = -\frac{(\boldsymbol{V}_p - \boldsymbol{U})}{\tau_p} + \boldsymbol{g} \tag{10}$$

where τ_p is the particle response time as given by:

$$\tau_p = \frac{m}{\frac{1}{2}\rho C_D(Re_p)A|\boldsymbol{V}_p - \boldsymbol{U}|} \tag{11}$$

For spherical particles in Stokes-type flows Eq. (11) then becomes:

(12) $$\tau_p = \frac{\rho_p d_p^2}{18\nu}$$

The vector Eq. (6) can be split in its three components as:

(13)
$$\frac{dV_{px}}{dt} = -\frac{(V_{px} - U_x)}{\tau_p}$$
$$\frac{dV_{py}}{dt} = -\frac{(V_{py} - U_y)}{\tau_p}$$
$$\frac{dV_{pz}}{dt} = -\frac{(V_{pz} - U_z)}{\tau_p} - g$$

A method for solving the three scalar equations is the one proposed in Ref.[8], according to which Eqs. (13) are re-written as:

(14)
$$\frac{d}{dt}\left(V_{px}e^{t/\tau_p}\right) = F_x(t)e^{t/\tau_p}$$
$$\frac{d}{dt}\left(V_{py}e^{t/\tau_p}\right) = F_y(t)e^{t/\tau_p}$$
$$\frac{d}{dt}\left(V_{pz}e^{t/\tau_p}\right) = F_z(t)e^{t/\tau_p}$$

with the terms:

$$F_x = \frac{U_x}{\tau_p}$$
$$F_y = \frac{U_y}{\tau_p}$$
$$F_z = \frac{U_z - g\tau_p}{\tau_p}$$

representing the forcing functions. The solution to this set of equations is obtained by applying a set of recurrence equations of the form:

(15)
$$\begin{aligned} &V_{p,i}(t+\Delta t) \\ &= V_{p,i}e^{-\Delta t/\tau_p} + e^{-(t+\Delta t)/\tau_p}\int_t^{t+\Delta t} F(\sigma)\, e^{\sigma/\tau_p} d\sigma \\ &= V_{p,i}e^{-\Delta t/\tau_p} + \tau_p\, F(t)\left(1 - e^{-\Delta t/\tau_p}\right) \end{aligned}$$

where $i = 1,2,3$ corresponding to the three x, y, z directions. This equation is accurate for any value of $\Delta t/\tau_p$ because no approximation is made for it. The only approximation involved regards the term $F(\sigma)$ which is assumed to remain constant during the period of time Δt.

Once evaluated the effective velocity $\boldsymbol{V}_p$ of each particle, the update of each particle's position $\mathbf{x}_p$ in space is obtained by applying a third-order Adams-Bashforth explicit scheme:

(16)
$$\boldsymbol{x}_p{}^{n+1} = \boldsymbol{x}_p{}^{n} + \left[23\boldsymbol{V}_p(t) - \mathbf{16}\boldsymbol{V}_p(t-\Delta t) + \mathbf{5}\boldsymbol{V}_p(t-2\Delta t)\right]\Delta t/12$$

4.4 Turbulent boundary layer

The potential nature of RAMSYS solver, centred on an inviscid model of the aerodynamics, enables the prediction of the external flow but does not resolve the near-wall boundary layer region. To overcome the problem, a turbulent boundary layer model, based on a self-similar logarithmic velocity profile, was applied, having the form of Eq.(3).

However, this equation does not consider the fluctuating component present in the flow field, which is required to properly simulate the entrainment process. A solution to the problem is illustrated by Haehnel et al. in Ref.[17], where the stochastic modelling proposed by Teunissen, Ref.[31], is described.

In this model, the instantaneous velocity component in the i-th direction can be written as $V_i = \bar{V}_i + V'_i$ where $\bar{V}_i$ is the mean value, evaluated by Eq.(3), and V'_i represents the fluctuation that is evaluated by using the stochastic model. It is useful to note that this evaluation is required only in the proximity to the ground, where the particle entrainment takes place, and not in the whole flow field. Following Teunissen, Ref.[31], the turbulence intensity $T_i = V'_i/\bar{V}_i$ in the atmospheric boundary layer (ABL) can be expressed as $T_{x,y} \approx 1/log\left(\frac{z}{z_0}\right)$ and $T_z \approx T_{x,y}/2$. Then, the fluctuation can be expressed as:

(17) $$V'_i = \zeta T_i$$

where ζ is a normally distributed random number varying between -1 and 1. Using Eq.(17), a fluctuating velocity component field for each of the coordinate directions near the surface at each time step is generated.

A drawback of this stochastic modelling of turbulence is that it does not capture the nature of real turbulent flow - that is, correlation in time and space - and the random stochastic fluctuations may not correctly transport the suspended particles since temporal correlations are neglected.

4.5 Calculation procedure

A *monolithic* approach was followed to numerically simulate the brownout, in the sense that the model for the particle transport was fully integrated in the aerodynamic solver RAMSYS.

In order to set up the computational procedure, the sketch of the aeolian sand transport, described by Wang et al. in Ref.[32], was used as a reference, and is illustrated in Figure 13. The ground soil consists of two layers: in the static layer, whose width is defined by the Nikuradse equivalent roughness length k_r, described in section 4.1, the particles are still and are not mobilized by the surface flow; the creep layer is a dense shear flow of particles driven by the shear stress τ, Eq. (2), applied on the surface of the creep layer. The interface region between the ground soil and the stream flow is represented by the outer layer, composed by the saltation layer, a dilute rapid particle flow in which heavier, saltating particles are accelerated by the stream flow before impacting the creep layer, and a suspension layer in which lighter particles are lofted into the air and remain in suspension.

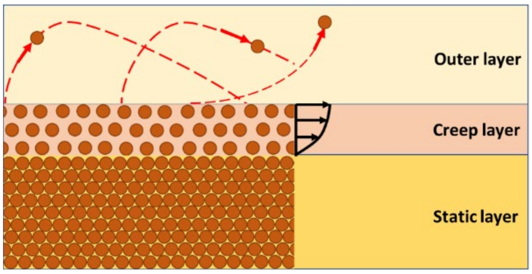

Figure 13: Sketch of the particle transport model

The simulation starts by reading the rotor geometry, the test conditions and the initial distribution of particles lying on a flat ground surface. Despite this initial distribution can be composed by particles of different granulometry (density and diameter) and different concentration, the simulations described in the present document refer to a uniform distribution of particles all having the same density and diameter.

The simulation proceeds by starting a time evolution of both the aerodynamic flow field and the brownout. In particular, for each time step, the following five points are executed:

1. Laplace's equation for the velocity potential φ, Ref.[21], is solved, and the pressure distribution and the loads acting on the rotor are evaluated;
2. The velocities on a surface at the outer edge of the boundary layer are calculated;
3. Depending on the position of each single particle at the current time step, three different conditions are possible:
    a. The particle is outside of the boundary layer, in the outer layer: in this case, the full particle convection model, described in section 4.3, is applied;
    b. The particle is inside the boundary layer but outside of the creep layer: in this case, the particle convection model of section 4.3 is applied with the constraint that the vertical particle velocity w_p is produced by the gravitational force and the flow turbulence;
    c. The particle is inside the boundary layer and inside the creep layer. In this case, the friction velocity u_* and the threshold friction velocity u_{*t} are evaluated. If $u_* > u_{*t}$ then the particle is uplifted with initial vertical velocity $w_p = 2.8u_{*t}$, according to Owen's hypothesis, Ref.[27]; otherwise, if $u_* \leq u_{*t}$, then $\boldsymbol{V}_p = 0$ and the particle remains still.
4. The particles' positions are updated: $\frac{d\mathbf{x}_p}{dt} = \boldsymbol{V}_p$;
5. A new time step is set: $t^{n+1} = t^n + \Delta t$ and the calculation is repeated from point 2.

4.6 Results of the brownout simulations

Brownout simulations were carried out for the helicopter rotor hovering at a height from the ground equal to one rotor blade radius ($z/R = 1$). The ground was modelled as a flat surface and its presence was simulated by applying the Method of Images (MIM). A $70\ m \times 70\ m$ portion of the ground surface, centred with the rotor hub, was disseminated with a single-layered, uniform distribution of 250000 particles of silica sand (density $\rho_p = 2650\ kg/m^3$), all having the same size. The thickness of the sand soil, z_{soil}, was set equal to $0.24\ m$, taking into account the considerations made by D'Andrea in Ref.[7], stating that the thickness value is about 1 foot ($0.3048\ m$), and by Syal in Ref.[9], according to which this value is about 2% of the rotor blade radius (i.e. $0.10\ m$ in the specific case). The initial vertical position of the particles was set equal to z_{soil}.

Six test cases were analysed, each with a different particle diameter:

- Dust particles: $1\mu m; 10\mu m; 50\mu m;$
- Sand particles: $100\mu m; 500\mu m; 1000\mu m$

Figure 14 illustrates the brownout cloud shapes after $3s$ of simulation for three particle diameters. In the case of $d_p = 1\mu m$, the gravitational forces are negligible but the inter-particle cohesive forces are so strong that the groundwash generated by the helicopter rotor is unable to entrain particles. Indeed, according to the values indicated in the diagram of Figure 10, the maximum value of the groundwash reached at the outer edge of the boundary layer, $u(\delta)$, is only about half the value of the velocity required to overcome the threshold friction velocity u_{*t} ($\sim 32\, m/s$ *vs* $\sim 68\ m/s$). Consequently, no particle is mobilized.

When the particle diameter is $d_p = 10\mu m$, Figure 14a, the gravitational forces are still small but the inter-particle forces exert a lower effect, as indicated in Figure 11. In this case, the velocity required to overcome u_{*t} becomes lower than the maximum value of $u(\delta)$ ($\sim 19\, m/s$ *vs* $\sim 32\ m/s$), and many particles, under the effect of the groundwash, are entrained from the ground and uplifted. The particles underneath the rotor hub are subject to the downwash of the rotor not yet converted into an outwash. For this reason, the friction velocity is extremely low and the particles stay still.

The case with particle diameter of $d_p = 100\mu m$, Figure 14b, is the one where u_{*t} reaches the minimum. The velocity required to overcome u_{*t} becomes much lower than the maximum value of $u(\delta)$ ($\sim 7\, m/s$ *vs* $\sim 32\ m/s$).

Sand particles with diameter $d_p = 1000\mu m$, Figure 14c, are dominated by the gravitational forces. They are extremely heavy but nevertheless the u_{*t} is sufficiently lower than the maximum value of $u(\delta)$ ($\sim 12\, m/s$ *vs* $\sim 32\ m/s$) to enable their mobilization. The particles, under the effect of the groundwash, start a saltation process during which, once uplifted, they quickly fall back to the ground because of their weight, producing smooth ballistic-like trajectories.

A detail of the process of brownout cloud formation is illustrated in Figure 15 for the case of sand particles having diameter $d_p = 100\mu m$. The sequence shows the brownout evolution every $1s$. In the first second of simulation, the particles are mobilized and spread outward from the rotor hub with only an incipient uplift. In the next second of simulation, the outward spreading continues and the uplift becomes significant. In particular, at $t = 2s$ particles are rolled up by the rotor wake and fall back to the ground This process continues during the last second of simulation.

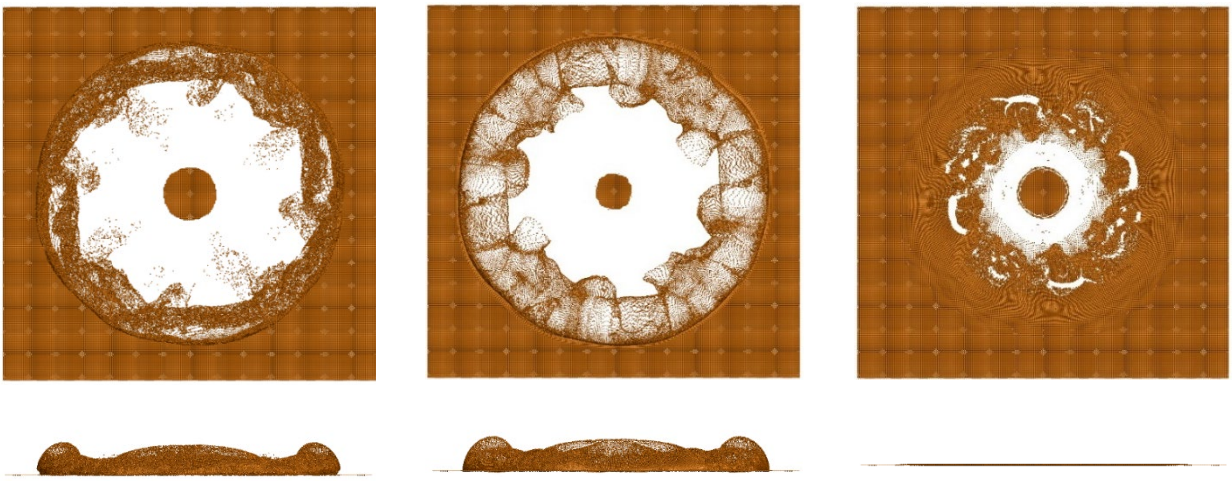

$a)\ d_p = 10\mu m$ $b)\ d_p = 100\mu m$ $c)\ d_p = 1000\mu m$

Figure 14: Brownout cloud development for particles of different diameters. Top view (top); Side view (bottom)

1.0s 2.0s 3.0s

Figure 15: Time evolution of the brownout cloud for particles of diameter $d_p = 100\mu m$.Top view (top); side view (bottom)

A quantification of the fraction of mobilized particles for the different particle diameters, after $2s$ and $3s$ of simulation, is shown in Figure 16. The maximum value is reached by sand particles of diameter $d_p = 100\mu m$.

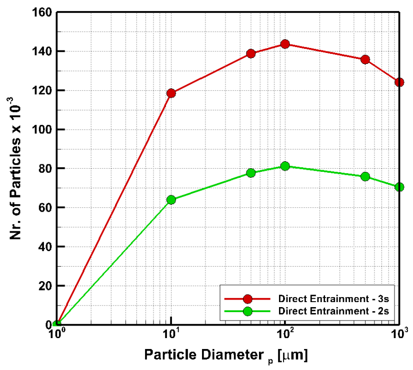

Figure 16: Fraction of mobilized particles as a function of particle diameter at $2s$ and $3s$

Figure 17 illustrates the fraction of mobilized particles distributions at the different heights from the ground, for the different particle diameters, after $3s$ of simulation. Each bar represents an altitude range of $0.25m$, having its upper boundary in the value indicated in the ordinates (e.g.: the bar corresponding to the abscissa $1m$, accounts for all the particles having a height from the ground from $0.75m$ to $1.00\ m$). With the only exception of the case $d_p = 1\mu m$, for which no mobilization of particles occurs, as the particle diameter increases, the particles are gradually more cconcentrated toward the ground. In particular, with reference to the position of the helicopter, Figure 18-left, particles of diameter $d_p = 10\mu m$ generate a brownout cloud that fully envelopes the helicopter but only a fraction of less than 5% can potentially obscure the visibility of the cabin (between $3m$ and $4m$). In addition, only 0.55% of particles are suspended in the region of the helicopter rotor (between $4.5m$ and $5m$). However, Figure 18-right shows that the cloud is sufficiently away from the helicopter to create visibility problems to the pilot or damages to the helicopter.

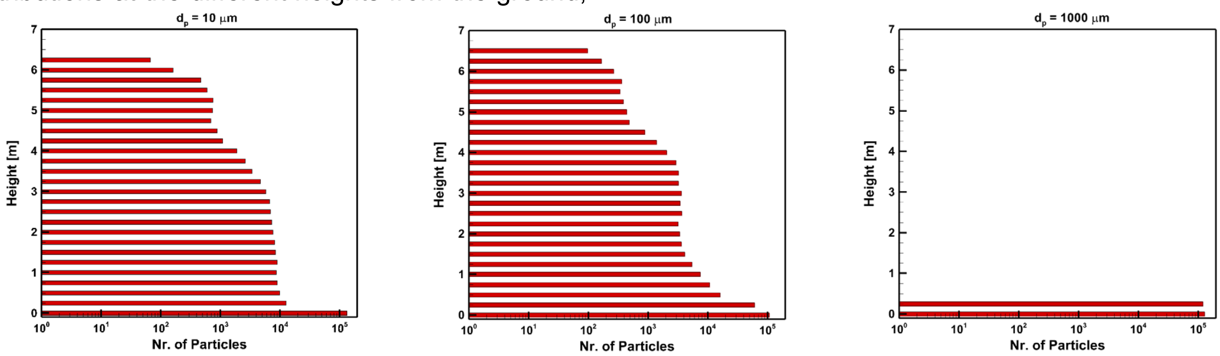

Figure 17: Fraction of mobilized particles *vs* particle height from the ground at 3 s of simulation

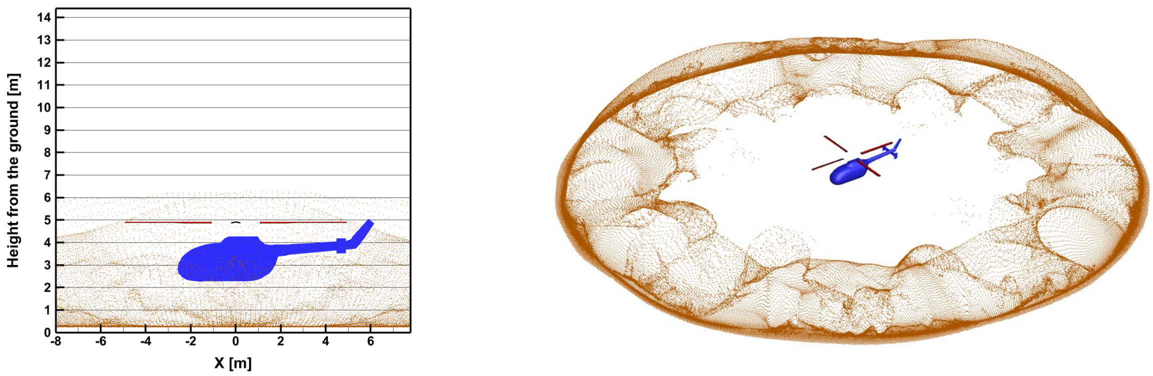

Figure 18: Brownout cloud around BO105 helicopter at 3 s of simulation using sand particles of diameter $d_p = 100\mu m$ – Side view – detail around the helicopter (left); Global view (right)

Figure 19 illustrates the average velocities reached by the fractions of mobilized particles, after $3s$ of simulation, for the different particle diameters. Since no particle of diameter $d_p = 1\mu m$ is mobilized, the average velocity is zero. For the particle diameter $d_p = 10\mu m$ about 23% of particles reach velocities between $10m/s$ and $14m/s$, whereas for the case $d_p = 100\mu m$ the same velocities are reached by about 35% of particles. At $d_p = 1000\mu m$, as the particles are much heavier, the velocities reduce significantly and the majority of them have a velocity between $2m/s$ and $4m$

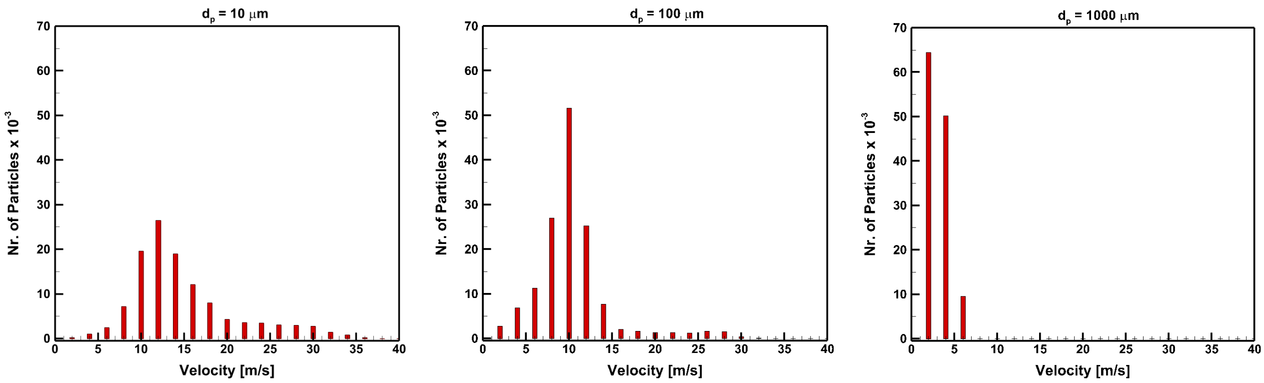

Figure 19: Fraction of mobilized particles *vs* particle velocities at 3 s of simulation

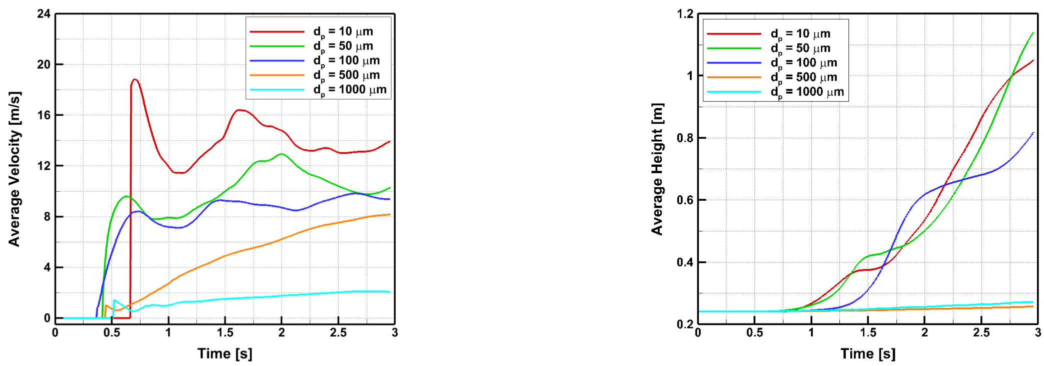

Figure 20: Average velocity (left) and height (right) of particles of various diameters in $3s$ of simulation

The time histories of the average height and velocities reached by the particles in the brownout clouds for the different particle diameters are illustrated in Figure 20. From the velocity diagram, it can be observed that the first particles to be mobilized are those having diameter $d_p = 100\mu m$, followed, in the order, by those with $d_p = 50\mu m, 500\mu m, 1000\mu m$, and finally by those with $d_p = 10\mu m$. This is fully in line with the respective values of the threshold friction velocities as shown in Figure 11. The average values suddenly increase and after some fluctuations tend to reach a plateau that is higher for the light particles of $d_p = 10\mu m$, for which the gravitational forces are still small and the inter-particle forces are less intense. The smallest particles of $d_p = 1\mu m$ stay still. The average heights follow the trends of the velocities but show an almost monotonic growth, which would imply a further increase in height as the simulations continued.

Finally, some examples of the trajectories followed by the particles are given in Figure 21. Four initial positions are shown, having increasing distances from the rotor hub. The six different particle diameters were considered.

Depending on the initial distance from the rotor hub, the particles having diameter between $10\mu m$ and $100\mu m$ show different behaviours. In particular:

a) starting from the initial position of $x = 6.10\ m$, the particles with $d_p = 10\mu m$ and $50\mu m$ are immediately uplifted, fall back to the ground and are then uplifted again. Instead, the particle with $d_p = 100\mu m$ initially creeps along the ground surface, is then uplifted and finally falls back to the ground;

b) starting from the initial position of $x = 12.55m$, the three particles are immediately uplifted but only the lighter one, with diameter $d_p = 10\mu m$ remains in suspension throughout the $3s$ of simulation, while the other two particles show a similar behaviour as for the initial position of $x = 6.10m$;

c) Further increasing the distance from the hub, at the initial position equal to $x = 3.57m$ and $y = 14.66\ m$, the three particles are immediately uplifted and remain in suspension;

d) at the highest distance from the hub, $x = 25.05m$ and $y = 0.07m$, only the lighter particles are uplifted, to a low height though, whereas the particle with diameter $d_p = 100\mu m$ shows the tendency to saltate only.

Finally, the heaviest particles, of diameter $d_p = 500\mu m$ and $1000\mu m$ clearly show a creeping or saltating behaviour, running shorter distances and reaching low heights as the initial position is farther from the rotor hub. A magnification of the saltation trajectory is shown in Figure 22

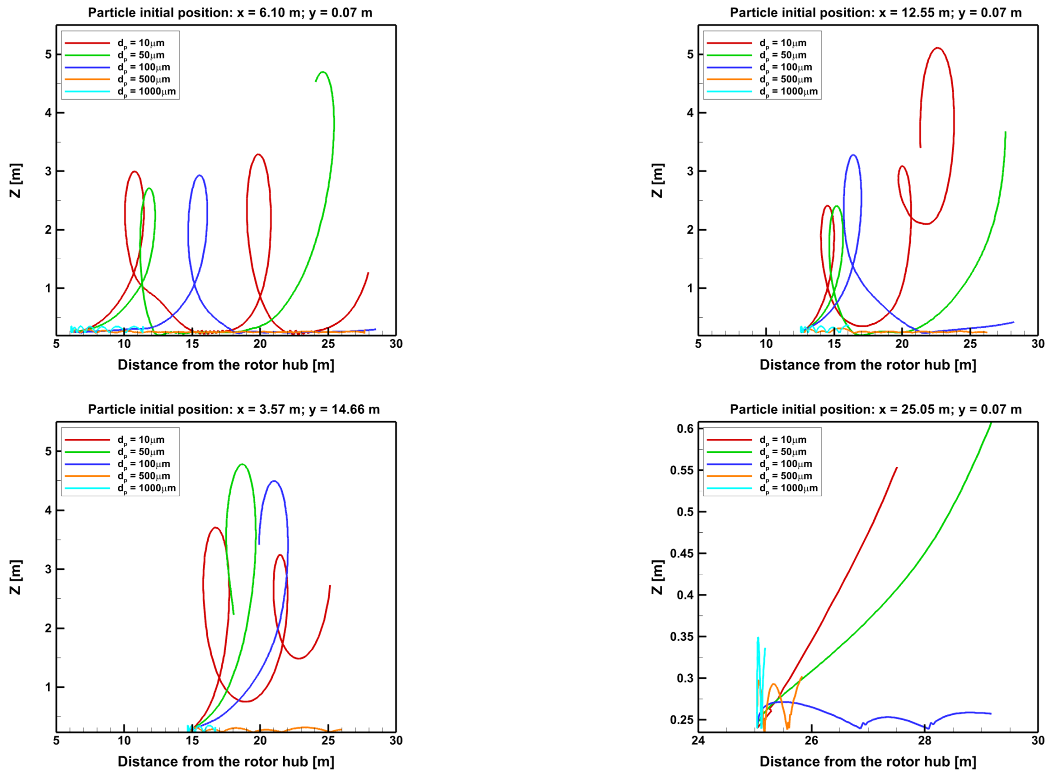

Figure 21: Trajectories of particles of various diameters, at different initial positions, in $3s$ of simulation.

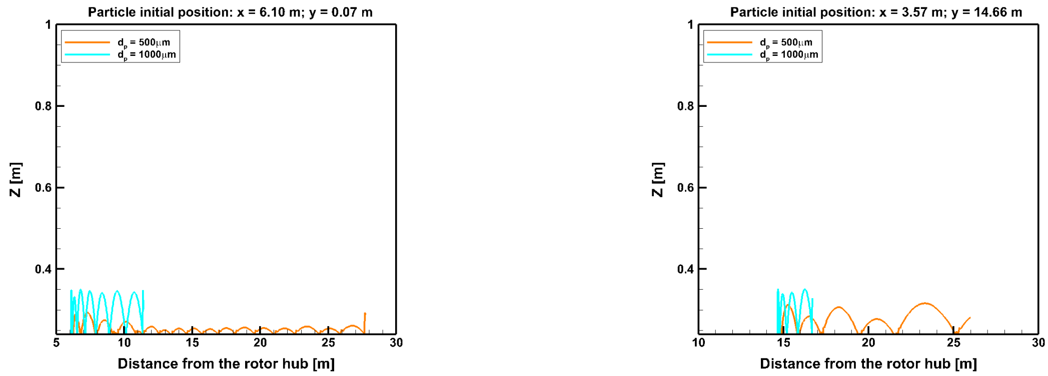

Figure 22: Saltation of the particle of diameter $d_p = 500\mu m$ and $d_p = 1000\mu m$ at two different initial positions in $3s$ of simulation

5 BOMBARDMENT

During its dynamic evolution, an entrained sediment particle might hit the ground due to the vortical flow of the rotor wake and the gravitational force. The impact forms a crater from which new particles are ejected, while the impacting particle itself first slides along the ground and then rebounds, Figure 23.

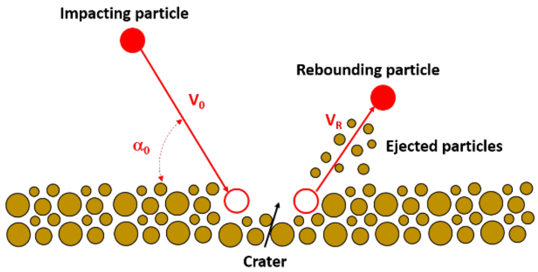

Figure 23: A sediment particle impacting the ground rebounds and generates a crater from which new particles are ejected

In turn, the rebounded and ejected particles may undergo the same process by hitting the ground and further ejecting new particles. This cascade effect is called bombardment and represents the main mechanism with which the brownout cloud is formed. To detail the phenomenon, three forms of bombardment can be identified: in the *saltation bombardment* the particles saltating on the sediment bed can eject more particles; in the *local re-ingestion bombardment*, suspended particles, trapped by the vortical flow are first uplifted and then bombarded back on the sediment bed, thus ejecting more particles; in the *global bombardment*, highly suspended particles may be re-ingested by the rotor disk and bombarded back to the ground under the strong effect of the rotor downwash.

Since a brownout cloud can be composed of tens of billions of particles per cubic meter, the computation of the motion of every single particle is computationally prohibitive. For this reason, a probabilistic approach is applied to investigate the problem.

The numerical model implemented in RAMSYS, is based on the model by Lu and Shao, Ref.[33], that gives a measure of the volume removal (crater) by impacting particles, and on the model by Syal and Leishman, Ref.[10], that evaluates the velocity of the rebounded particle and the ejected particles starting from the velocity of the impacting particle. The description of the two models is illustrated in the following.

5.1 Volume of crater and number of particles ejected

The volume ϑ of the crater formed by the impacting particle, having velocity $\boldsymbol{V}_0$ and inclination α_0 with respect to the ground surface, is evaluated by Lu and Shao, Ref.[33], by solving the equation of motion for ploughing particles:

$$\vartheta = \frac{\pi \rho_p d_p^3 |\boldsymbol{V}_0|^2}{12 P_s} \left(\sin 2\alpha_0 - 4 \sin^2 \alpha_0 + \frac{7.5\pi |\boldsymbol{V}_0| \sin^3 \alpha_0}{\beta_v d_p} \right) \quad (18)$$

where $\beta_v = \sqrt{2 P_s d_P / m_0}$.

P_s represents the plastic pressure of the soil on the particle, and its value ranges between 10 to $25\ x\ 10^{-5}\ N/m^2$. The value used in the present simulations was set equal to $1000\ N/m^2$ as also used by Lu and Shao for smooth and fine-grained unaggregated sediment beds.

The number of particles N_B ejected by the impingement of a single particle is evaluated by dividing the volume of the crater ϑ by the volume of the particle:

$$N_B = \frac{6\vartheta}{\pi d_p^3} \quad (19)$$

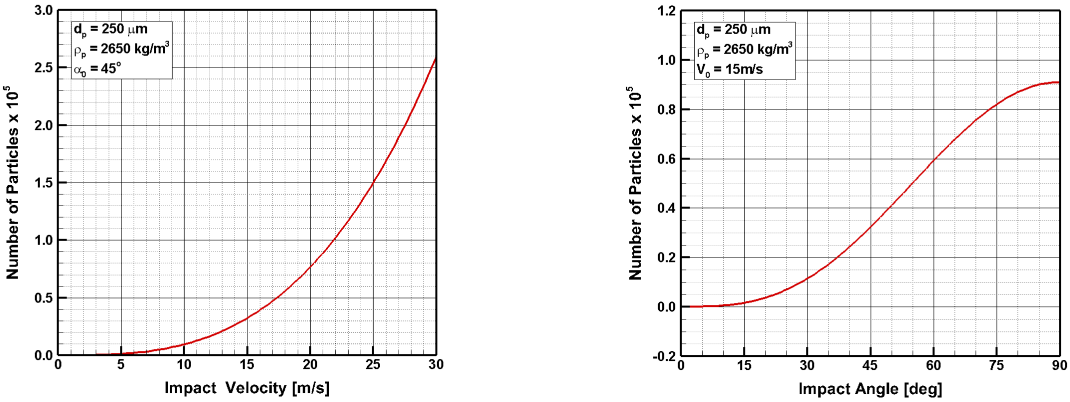

Figure 24: Number of particles ejected by a particle having diameter $d_p = 250\ \mu m$ and density $\rho_p = 2650\ kg/m^3$by varying the impact velocity at a given impact angle (left); and the impact angle at a given impact velocity (right)

Figure 24 illustrates an example of the number of particles ejected by an impacting particle obtained by using Eqs.(18) and (19). In particular, Figure 25 illustrates the number of particles ejected by a particle having assigned impact velocity, impact angle, density, and variable diameter, as a function of the diameter of the particles lying on the sediment bed. The figure highlights that the particles having a diameter of 1 and $10\ \mu m$, when impacting the ground, can eject particles of diameter not greater than 50 and 350 μm, respectively.

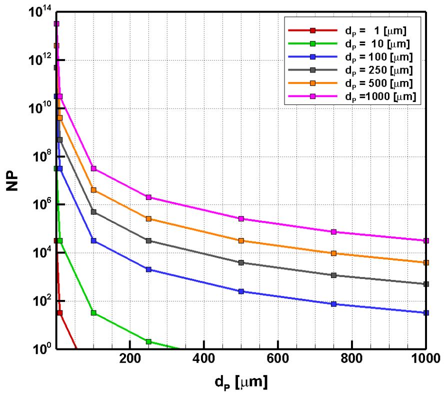

Figure 25: Number of particles ejected by a particle having assigned impact velocity, angle and density and variable diameter, as a function of the diameter of the particles lying on the sediment bed

5.2 Initial velocity of the rebounded and ejected particles

The evaluation of the initial velocity of the rebounded and ejected particles during bombardment was carried out by making a set of simplifying assumptions and approximations. In particular, the impacting particle does not shatter when it hits the ground, and all the ejected particles are assumed to have the same diameter and density as the impacting particle. This simplifying assumption makes the modelling of the bombardment process much easier to approach than considering particles of different diameters and densities, as would happen in reality.

When the impacting particle hits the ground with velocity $\boldsymbol{V}_0$, it is subjected to a compression, then to a creeping phase, and finally rebounds. The dynamic of the process is described by the set of Eqs.(20):

$$\begin{aligned} V_{R_x} &= V_{0_x} + \varepsilon_x f(1+e) V_{0_z} \\ V_{R_y} &= V_{0_y} + \varepsilon_y f(1+e) V_{0_z} \\ V_{R_z} &= -e V_{0_z} \end{aligned} \quad (20)$$

where $\varepsilon_x = V_{0_x} / \sqrt{{V_{0_x}}^2 + {V_{0_y}}^2}$ and $\varepsilon_y = V_{0_y} / \sqrt{{V_{0_x}}^2 + {V_{0_y}}^2}$.

These equations express the three components of the rebounding velocity mainly as a function of the vertical velocity of the impacting particle. The

Coulomb frictional force that the ground exerts on the particle during the creeping phase is expressed by the frictional coefficient f, which, for silica particles, assumes the value of 0.14. The coefficient e is the coefficient of restitution that expresses how much of the impacting vertical velocity is recovered thanks to the elasticity of the particle after the impact: $e = \left|V_{R_z}/V_{0_z}\right|$. This value has been set equal to 0.6 as also used by Syal et al., Ref.[10].

The velocities of the $\mathrm{N_B}$ ejected particles were evaluated by following a probabilistic approach described in the following.

It was assumed that these velocities are distributed normally according to the following trivariate normal distribution:

$$\Phi(\boldsymbol{\mu}_B, \boldsymbol{\Sigma}_B) = \frac{1}{(2\pi)^{3/2}|\boldsymbol{\Sigma}_B|^{1/2}} exp\frac{-1}{2}\left[(\boldsymbol{V}_n - \boldsymbol{\mu}_B)^T {\boldsymbol{\Sigma}_B}^{-1}(\boldsymbol{V}_n - \boldsymbol{\mu}_B)\right] \tag{21}$$

This distribution depends on $\boldsymbol{\mu}_B$ and $\boldsymbol{\Sigma}_B$ that are the mean and covariance matrices of the distribution, respectively:

$$\boldsymbol{\mu}_B = \frac{1}{N_B + 1}\sum_{n=1}^{N_B+1} \boldsymbol{V}_n \tag{22}$$

$$\boldsymbol{\Sigma}_B = \begin{bmatrix} \sigma_{xx}^2 & \sigma_{xy}^2 & \sigma_{xz}^2 \\ \sigma_{yx}^2 & \sigma_{yy}^2 & \sigma_{yz}^2 \\ \sigma_{zx}^2 & \sigma_{zy}^2 & \sigma_{zz}^2 \end{bmatrix} \tag{23}$$

where each element of the covariance matrix is the variance of the i-th dimension with the j-th one and is expressed as:

$$\sigma_{ij}^2 = \frac{1}{N_B + 1}\sum_{n=1}^{N_B+1} \left(V_{n_i} - \mu_{B_i}\right)\left(V_{n_j} - \mu_{B_j}\right) \tag{24}$$

The evaluation of $\boldsymbol{\mu}_B$ and $\boldsymbol{\Sigma}_B$ is therefore necessary to calculate the velocities $\boldsymbol{V}_n$ of the ejected particles. For this purpose, it was applied the conservation of the momentum equation that links momentum of the rebounding particle to that of the ejected particles:

$$m_R \boldsymbol{V}_R = \sum_{n=1}^{N_B+1} m_n \boldsymbol{V}_n \tag{25}$$

The simplifying assumption of particles of the same density and diameter, $m_R = m_n$, transforms this equation into a simple relation between velocities.

Eq.(22) allows the evaluation of the mean matrix $\boldsymbol{\mu}_B$ by knowing the value of the velocity $\boldsymbol{V}_R$ of the rebounded particle:

$$\boldsymbol{\mu}_B = \frac{1}{N_B + 1}\sum_{n=1}^{N_B+1} \boldsymbol{V}_n = \frac{\boldsymbol{V}_R}{N_B + 1} \tag{26}$$

To evaluate the covariance matrix $\boldsymbol{\Sigma}_B$, the conservation of the kinetic energy was applied. More specifically, it was assumed that the kinetic energy of the impacting particle was in part dissipated in the form of heat during the creep phase, and that the remaining part was equally subdivided as kinetic energy E_R of the rebounding particle and kinetic energy of the ejected particles, according to the equation:

$$E_R = \frac{1}{2} m_R |\boldsymbol{V}_R|^2 = \frac{1}{2}\sum_{n=1}^{N_B+1} m_n |\boldsymbol{V}_n|^2 \tag{27}$$

Also in this case, the assumption of equal density and diameter between the rebounding particle and the ejected ones makes Eq.(27) a simple relation between velocities.

A further simplification was made by considering the covariance matrix $\boldsymbol{\Sigma}_B$ fully diagonal, thus assuming that the three dimensions are not coupled.

$$\boldsymbol{\Sigma}_B = \begin{bmatrix} \sigma_{xx}^2 & 0 & 0 \\ 0 & \sigma_{yy}^2 & 0 \\ 0 & 0 & \sigma_{zz}^2 \end{bmatrix} \tag{28}$$

The expression of the generic diagonal element σ_{ii}^2 is given by:

$$\sigma_{ii}^2 = \frac{1}{N_B + 1}\sum_{n=1}^{N_B+1} \left(V_{n_i} - \mu_{B_i}\right)^2 = \frac{1}{N_B + 1}\sum_{n=1}^{N_B+1} \left({V_{n_i}}^2 - 2V_{n_i}\mu_{B_i} + {\mu_{B_i}}^2\right) \tag{29}$$

which, for each of the three dimensions, considering Eqs.(26), (27) and (29), can be rearranged as:

$$\begin{aligned} \sigma_{xx}^2 &= \frac{2E_R}{m_R(N_B + 1)} \frac{{V_{R_x}}^2}{{V_{R_x}}^2 + {V_{R_y}}^2 + {V_{R_z}}^2} - \frac{{V_{R_x}}^2}{(N_B + 1)^2} \\ \sigma_{yy}^2 &= \frac{2E_R}{m_R(N_B + 1)} \frac{{V_{R_y}}^2}{{V_{R_x}}^2 + {V_{R_y}}^2 + {V_{R_z}}^2} - \frac{{V_{R_y}}^2}{(N_B + 1)^2} \end{aligned} \tag{30}$$

$$\sigma_{zz}^2 = \frac{2E_R}{m_R(N_B+1)} \frac{{V_{R_z}}^2}{{V_{R_x}}^2 + {V_{R_y}}^2 + {V_{R_z}}^2} - \frac{{V_{R_z}}^2}{(N_B+1)^2}$$

Once calculated the mean and covariance matrices $\boldsymbol{\mu}_B$ and $\boldsymbol{\Sigma}_B$, the ejected velocities were evaluated by using the Box-Muller algorithm, Ref.[34], for each of the three dimensions.

5.3 Analysis of the results

The analyses of bombardment were carried out for six particle diameters: $1\,\mu m$, $10\,\mu m$, $50\,\mu m$, $100\,\mu m$, $500\,\mu m$ and $1000\,\mu m$ and for a duration of $2.2s$, corresponding to 14 rotor revolutions. This limitation was imposed by the extremely high number of particles generated in some cases, which made it prohibitive, in terms of computational time, to continue the runs. The test conditions were the same as for the analysis of the direct entrainment condition only.

Figure 26 shows the results in terms of the number of particles mobilised as a function of particle diameter, after $2.2s$ of simulation. The changes in particle diameters produce order-of-magnitude differences in the amounts of newly generated particles, the maximum, $O(10^7)$, reached at $d_p = 100\mu m$, as also obtained in the simulations without bombardment. Instead, no mobilisation of particles is shown for $1\mu m$ particles, as already observed in the simulations without bombardment, thus indicating that, at least for the test conditions investigated, the friction velocity produced by the rotor flow is not sufficient to break the high inter-particle forces.

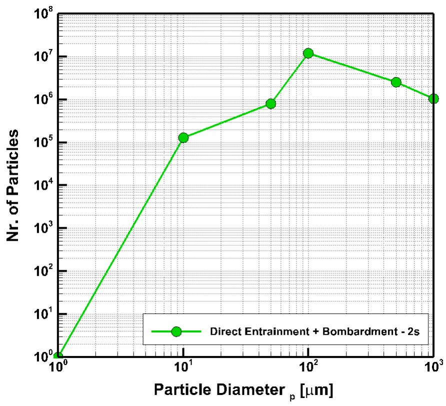

Figure 26: Number of mobilised particles as a function of particle diameter at $2.2s$

The evolution in time of the number and nature of particles generated during the brownout is illustrated in Figure 27. It refers to the case with particles of diameter $100\,\mu m$, which produced the largest number of particles, equal to about 17 million, during the last time step of the simulation. Each particle was tagged to distinguish the nature of its entrainment mechanism.

Before the start of the bombardment phase, the particles are uplifted under the effect of the shear stress exerted by the vortical flow on the ground surface. This is the direct entrainment, which begins after about $0.38s$ from the start of the simulation. In this phase, no additional particles are generated, and those mobilised either remain within the boundary layer, some inside the creep layer, some outside, or are suspended in the flow. About $0.10s$ later, the bombardment begins: some particles, once they hit the ground, rebound and generate new particles. Initially, this phase presents some fluctuations where the process of particle rebound and ejection is slowed down or accelerated. However, after about $1s$, a purely exponential phase begins. Furthermore, the figure shows that a significant part of the ejected particles remains confined within the boundary layer but outside the sediment bed.

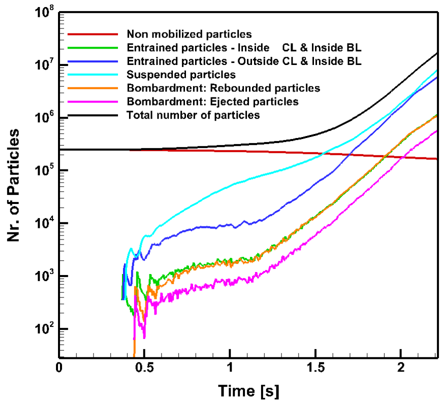

Figure 27: Evolution in time of the number and nature of $100\,\mu m$ particles generated during the brownout

Figure 28 shows a detail of the cloud of $100\,\mu m$ particles generated during the brownout, with or without simulation of the bombardment. In particular, the comparison highlights that no change in the shape and extension of the two clouds can be globally identified. Instead, a significant difference can be observed regarding the concentration of particles, mainly toward the lower part of the cloud. These two features would suggest the following two considerations:

1. Any simulation focused on the evaluation of the particle cloud shape and spatial extension can avoid the modelling of the bombardment, thus saving an enormous amount of computational time;
2. Conversely, the bombardment is essential if its simulation is required to make subsequent evaluations about the obscuration effects produced by the brownout cloud.

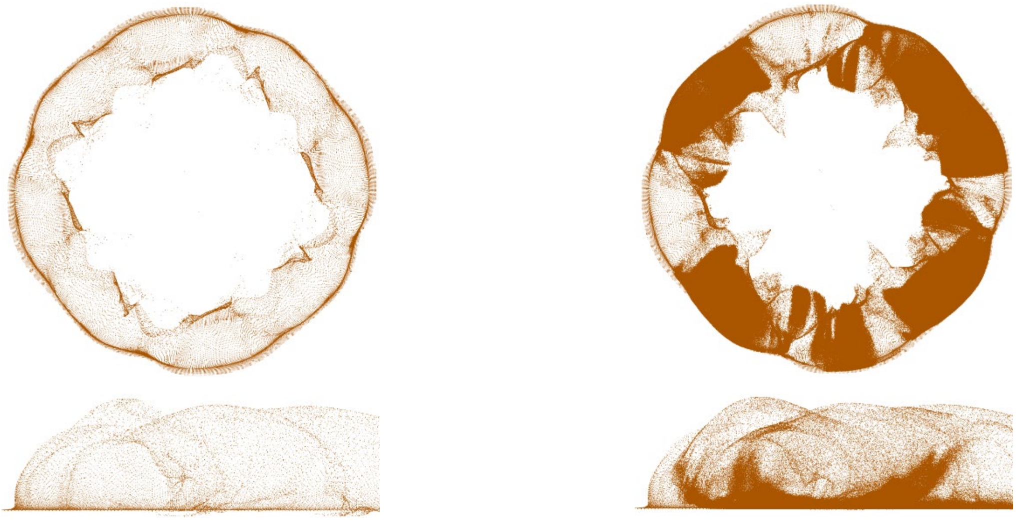

Figure 28: Cloud of $100\ \mu m$ particles generated during the brownout. Top view (top); detail of the side view (bottom): without bombardment (left); with bombardment (right)

A comparison of the simulations with and without bombardment, for particles of $100\ \mu m$ of diameter, is shown in Figure 29 in terms of the number of mobilised particles vs particle height from the ground and velocities at $2.2s$ of simulation. The simulation of the bombardment, as previously discussed, does not change the distribution of the particles at the several heights from the ground, but greatly increases the number of particles entrained. Instead, the effect on the particle velocities is significant, as higher velocities, up to $34\ m/s$, are reached by modelling the bombardment.

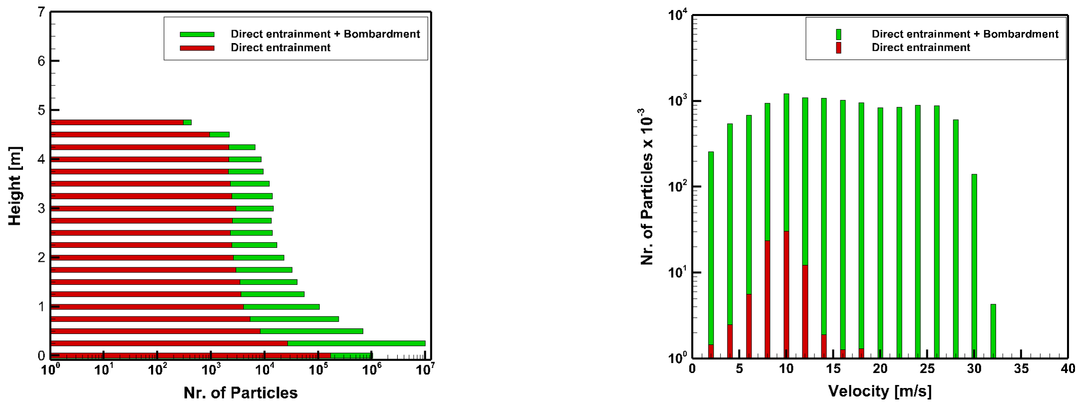

Figure 29: Number of mobilised $100\ \mu m$ particles vs particle height from the ground (left) and velocities (right) at $2.2s$ of simulation

6 EXAMPLE OF BROOWNOUT FOR MULTIROTOR CONFIGURATIONS

The brownout of two multirotor configurations was simulated to evaluate their influence on the density and extension of the generated cloud. Only the direct entrainment model was considered, for a particle diameter of $d_p = 100\mu m$.

6.1 Counter-rotating rotors

The brownout of two counter-rotating rotors in ground effect was simulated. Each rotor consisted of two blades, the same as those of the four-bladed rotor used for the nominal investigations, and set at the same collective pitch. The vertical distance between the two rotors was set at 10% of the rotor radius, while the distance from the ground was set at $z/R = 1$, measured with respect to the mean distance between the two rotors. The rotor speed was the same as the nominal four-bladed rotor.

Figure 30 shows a more non-isotropic shape of the toroidal cloud generated by the counter-rotating rotors in comparison with the one produced by the nominal four-bladed rotor. Despite this difference, their horizontal and vertical dimensions remain comparable.

Figure 31-left shows that the nominal rotor uplifts particles up to a slightly higher distance from the ground. Instead, the counter-rotating rotors accelerate more particles to the speed of $10\ m/s$, as shown in Figure 31-right.

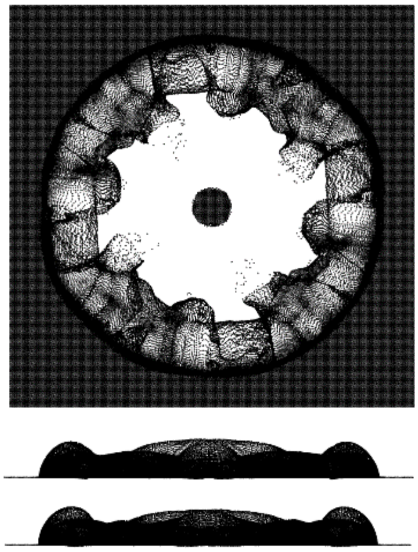

Figure 30: Brownout cloud (Top view - top; Side views: YZ – centre; XZ - bottom) generated by the counter-rotating rotors (brown circles) and compared to the one produced by the nominal four-blade rotor (black circles).

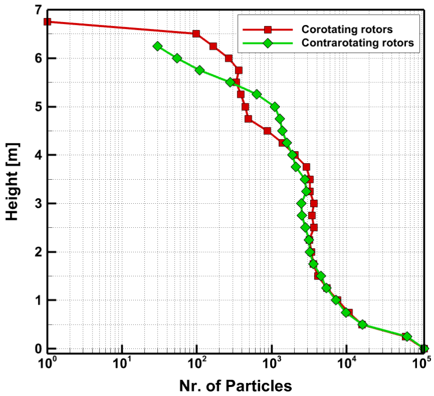

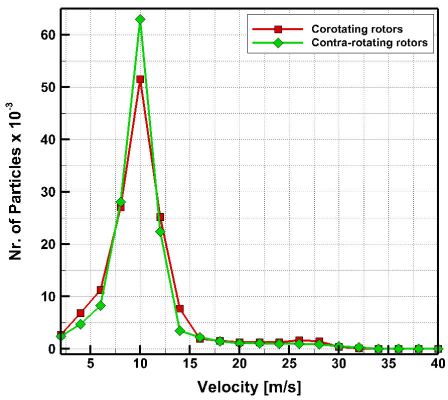

Figure 31: Number of mobilised $100\ \mu m$ particles vs particle height from the ground (left) and velocities (right) at $3s$ of simulation

6.2 Side-by-side rotors

The brownout of two side-by-side rotors in ground effect was also simulated. Each rotor consisted of two blades, the same as those of the four-bladed rotor used for the nominal investigations, and set at the same collective pitch. The distance between the two rotor hubs was set at 1.2 rotor diameters, while the distance from the ground was set at $z/R = 1$. The rotor speed was the same as the nominal four-bladed rotor. The number of particles was set equal to 640000 in consideration of the larger area of the two rotor disks. The analysis was conducted with the rotors in both co-rotating and counter-rotating configurations.

Figure 32: Top view of the time evolution, from left to right, of the brownout cloud generated by side-by-side counter-rotating rotors (top) and co-rotating rotors (bottom) after $1.5s$; $2.5s$; and $3s$, respectively.

Figure 32 illustrates the time evolution, from left to right, of the brownout cloud generated by side-by-side counter-rotating rotors (top) and co-rotating rotors (bottom) after $1.5s$; $2.5s$; and $3s$, respectively. It reveals that the particles initially lying between the two rotor disks (e.g. after $1.5s$) are progressively washed outward by the wake system of the side-by-side rotors, and the particle uplift in this region is extremely reduced.

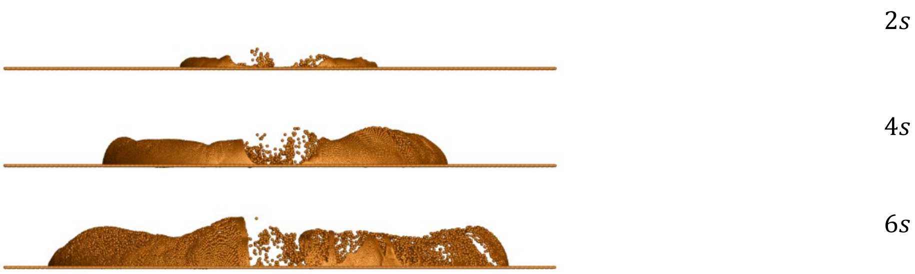

Figure 33: Side view of the brownout cloud generated by side-by-side counter-rotating rotors after $2s$, $4s$ and $6s$

This behaviour is more clearly illustrated by the side view of the brownout cloud displayed in Figure 33. Specifically, even when the simulation time is doubled, the brownout cloud shows a region of reduced uplift between the two rotors.

Similarly to what was already observed for the coaxial rotors, Figure 34-left shows that side-by-side co-rotating rotors uplift particles up to a slightly higher distance from the ground, whereas the side-by-side counter-rotating rotors accelerate more particles to the speed of $10\ m/s$, as shown in Figure 34-right.

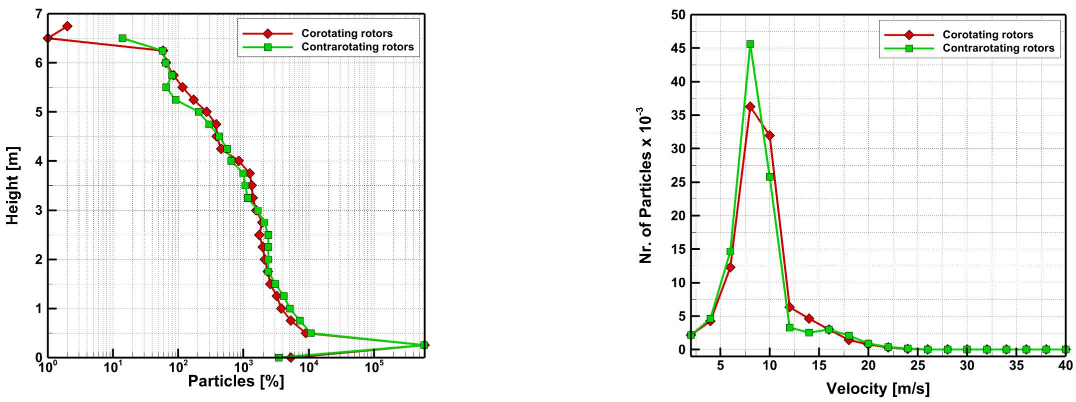

Figure 34: Side-by-side rotors: Number of mobilised $100\ \mu m$ particles vs particle height from the ground (left) and velocities (right) at $3s$ of simulation

7 CONCLUSIONS & FUTURE DEVELOPMENTS

A Lagrangian approach was implemented in the CIRA free-wake aerodynamic solver RAMSYS for the numerical simulation of the brownout phenomenon.

The full-scale four-bladed main rotor of the Bo105 helicopter was set in HIGE conditions, at a height from the ground equal to one blade radius ($z/R = 1$) and was trimmed to produce the thrust necessary to counterbalance the helicopter weight. The presence of the ground was simulated by the application of the Method of the Images (MIM). The flow field generated by the rotor was investigated in terms of loads and velocities induced on the ground surface and on a cross-sectional plane passing through the rotor hub centre. In order to demonstrate the capability of RAMSYS to correctly evaluate the flow field characteristics in ground effect, additional calculations were made on a small-scale isolated rotor, for which experimental results were available. A satisfactory numerical-experimental agreement was found.

The particle transport model was implemented by following a time-marching Lagrangian approach. The simulations were made for a total amount of time of $3s$ by using particles of silica sand having density equal to 2650 kg/m^3, and six different diameters: $1\mu m; 10\mu m; 50\mu m; 100\mu m;\ 5000\mu m; 1000\mu m$. Six runs were made, one for each particle diameter, in which particles of the same diameter were initially uniformly distributed on a flat ground surface, and their evolution in time, under the effect of the flow field produced by the rotor, was investigated.

The implemented particle transport model enabled the investigation of the particle entrainment, uplift, saltation and suspension phases. The results obtained showed the following characteristics:

1. The smallest particles ($d_p = 1\mu m$), despite their lowest weight, were not mobilized by the groundwash generated by the rotor because of the extremely high inter-particle cohesive forces;
2. Particles with diameter $d_p = 10\mu m$ were uplifted and remained in suspension thanks to their light weight and lower effect of the inter-particle forces. They produced a toroidal brownout cloud all around the helicopter rotor. Nevertheless, their concentration in the region of the helicopter cockpit was sufficiently low to avoid visibility problems to the pilot. The majority of the particles reached a time-averaged velocity between $10m/s$ and $14\ m/s$;

3. Particles with diameter $d_p = 100\mu m$, characterized by the lowest threshold friction velocity, were uplifted, but showed the tendency to fall back to the ground because of their weight. As such, a large concentration of particles remained confined within 0.50m from the ground. As for the previous case, the majority of the particles reached a time-averaged velocity between 10m/s and 14 m/s.
4. The heaviest particles, having diameter $d_p = 1000\mu m$, were accelerated by the stream flow following smooth ballistic-like trajectories in a layer $0.25m$ thick above the ground;
5. The results obtained after $3s$ of simulation did not highlight serious brownout problem for the investigated rotor for any granulometry of the particles. Nevertheless, a more long-lasting simulation might produce more severe brownout conditions;
6. The particle bombardment was implemented by following the models proposed by Lu and Shao to evaluate the volume removal (crater) caused by the impacting particles, and by Syal and Leishman to probabilistically assess the dynamics of new particles generated by the collision of the incoming particles with the ground. In this context, the difference from the brownout model, only implementing a direct entrainment mechanism, proved to be significant. Indeed, millions of new particles were generated, particularly in the case involving particles of $100\mu m$. Given the enormous number of new particles, the calculations were limited to 2.2 seconds of simulation, as the computational time and memory requirements became prohibitive. Nevertheless, the analysis of the results obtained led to the following conclusions:
    a. Any simulation focused on the evaluation of the particle cloud shape and spatial extension can avoid the modelling of the bombardment, thus saving an enormous amount of computational time;
    b. Conversely, the bombardment is essential if its simulation is required to make subsequent evaluations about the obscuration effects produced by the brownout cloud.

The brownout generated by two multirotor configurations - coaxial rotor and side-by-side rotors - was simulated under the same HIGE and operational conditions as the nominal four-bladed rotor. Little differences with respect to the nominal case were found for the former configuration. Conversely, the side-by side configuration, regardless of the sense of rotation of the two rotors, highlighted a region with few particles between the two rotor hubs.

The future developments of the methodology will focus on the parallel implementation in RAMSYS of the bombardment mechanism, by using the Message Passage Interface (MPI), and on the application of a suitable particle clustering technique to enable a longer and more detailed simulation of the brownout.

8 ACKNOWLEDGMENTS

The numerical investigations described in the present paper were all carried out by the author in the framework of the CIRA programme TEDS: “TEcnologie e Dimostratori per l’esplorazione Spaziale” included in the National Aerospace Research Program (PRO.RA) approved by the Italian Ministry of University & Research, MUR.

9 REFERENCES

[1] Johnson, B., Leishman, J.G., Sydney, A., “Investigation of Sediment Entrainment in Brownout Using High Speed Particle Image Velocimetry,” presented at the 65th Annual National Forum of the American Helicopter Society, Inc., May 27–29, 2009, Grapevine, TX, USA;

[2] Ghosh, S., Rajagopalan, R.G., “A Computational Study on Rotor and Fuselage Configuration Effect on Rotorcraft Brownout,” Journal of the American Helicopter Society, Vol.67, 012001, 2022;

[3] Nathan, N., and Green, R., “Measurements of a Rotor Flow in Ground Effect and Visualization of the Brown-Out Phenomenon,” Proceedings of the 64th Annual Forum of the American Helicopter Society International, Montreal, Canada, April 29–May 1, 2008;

[4] Ramasamy, M., Potsdam, M., and Yamauchi, G. K., “Measurements to Understand the Flow Mechanisms Contributing to Tandem-Rotor Outwash,” Proceedings of the 71st Annual Forum of the American Helicopter Society International, Phoenix, AZ, May 5–7, 2015;

[5] Keller, J. D., Whitehouse, G. R., Wachspress, D. A., Teske, M., and Quackenbush, T., "A Physics Based Modeling of Helicopter Brownout for Piloted Simulation Applications," Proceedings of the 62nd Annual Forum of the American Helicopter Society International, Phoenix, AZ, May 2006;

[6] Wachspress, D. A.,Whitehouse, G. R.,Keller, J. D.,Yu, K.,Gilmore, P., Dorsett, M., and McClure, K., "A High Fidelity Brownout Model for Real-Time Flight Simulations and Trainers," Proceedings of the 65th Annual Forum of the American Helicopter Society International, Grapevine, TX, May 27–29, 2009;

[7] D'Andrea, A., "Numerical Analysis of Unsteady Vortical Flows Generated by a Rotorcraft Operating on Ground: A First Assessment," Proceedings of the 65th Annual Forum of the American Helicopter Society International, Grapevine, TX, May 27–29, 2009;

[8] Syal, M., Govindarajan, B., Leishman, J.G., "Mesoscale Sediment Tracking Methodology to Analyze Brownout Cloud Developments," presented at the 66th Annual Forum of the American Helicopter Society, Phoenix, AZ, USA, May 10–13, 2010;

[9] Syal, M., "Development of a Lagrangian-Lagrangian Methodology to Predict Brownout Dust Clouds," Ph.D. Thesis, University of Maryland, College Park, MD, 2012;

[10] Syal,M., and Leishman, J. G., "Modeling of Bombardment Ejections in the Rotorcraft Brownout Problem," AIAA Journal, Vol. 51, April 2013 pp. 849–866, DOI: 10.2514/1.J051761;

[11] Syal,M., and Leishman, J. G., "Predictions of Brownout Dust Clouds Compared to Photogrammetry Measurements," Journal of the American Helicopter Society, 58, 022001 (2013), DOI: 10.4050/JAHS.58.022001;

[12] Govindarajan, B., and Leishman, J., "Predictions of Rotor and Rotor/Airframe Configurational Effects on Brownout Dust Clouds," Journal of Aircraft, Vol. 53, March 2016, pp. 545–560, 2016, DOI:10.2514/1.C033447;

[13] Thomas, S., Kalra, T., and Baeder, J., "A Hybrid CFD Methodology to Model the Two-Phase Flowfield Beneath a Hovering Laboratory Scale Rotor," Proceedings of 30th AIAA Applied Aerodynamics Conference, New Orleans, LA, 2012, 25 June 2012 – 28 June 2012, Paper no: AIAA 2012-2911, DOI: 10.2514/6.2012-2911;

[14] Govindarajan, B., Leishman, J. G., and Gumerov, N. A., "Particle-Clustering Algorithms for the Prediction of Brownout Dust Clouds," AIAA Journal, Vol. 51, May 2013, pp. 1080–1094, DOI: 10.2514/1.J051907;

[15] Tan, J.F., Gao, J., Barakos, G., Lin, C.L., Zhang, W.G., Huang, M.Q., "Novel approach to helicopter brownout based on vortex and discrete element methods," Aerospace Science and Technology, 116, 106839. (doi.org/10.1016/j.ast.2021.106839);

[16] Ryerson, C., Haehnel, R., Koenig, G., and Moulton, M., "Visibility Enhancement in Rotorwash Clouds," AIAA-2005-263, Proceedings of 43rd AIAA Aerospace Sciences Meeting and Exhibit, Reno, NV, January 10–13, 2005;

[17] Haehnel, R., Moulton, M., Wenren, Y., and Steinhoff, J., "A Model to Simulate Rotorcraft-Induced Brownout," Proceedings of the 64th Annual Forum of the American Helicopter Society International, Montreal, Canada, April 29–May 1, 2008;

[18] Phillips, C., and Brown, R. E., "Eulerian Simulation of the Fluid Dynamics of Helicopter Brownout," Journal of Aircraft, Vol. 46, July 2009, pp. 1416–1429, DOI: 10.2514/1.4, 1999;

[19] Phillips, C., and Brown, R., "The Effect of Helicopter Configuration on the Fluid Dynamics of Brownout," Proceedings of the 34th European Rotorcraft Forum, Liverpool, UK, September 16–19, 2008;

[20] Rovere, F., Barakos, G., Steijl, R., "Comparison between Eulerian and Lagrangian methods to predict brownout clouds," Aerospace Science and Technology, 137, 108306. (doi: 10.1016/j.ast.2023.108306);

[21] Visingardi, A.; D'Alascio, A.; Pagano, A.; Renzoni, P. Validation of CIRA's Rotorcraft Aerodynamic Modelling SYStem with DNW Experimental Data. Proceedings of 22nd

European Rotorcraft Forum, Brighton, UK, 1996;

[22] Lehmann, P., “Bo105: Configuration Data,” GARTEUR AG23 document, 2015;

[23] Cheeseman, I.C., Bennett, W.C., “The Effect of the Ground on a Helicopter Rotor in Forward Flight,” Aeronautical Research Council Technical Report R&M No. 3021, London, 1957;

[24] Lee, T.E., Leishman, J.G., Ramasamy, M., “Fluid Dynamics of Interacting Blade Tip Vortices with a Ground Plane,” presented at the 64th Annual Forum of the American Helicopter Society, Montreal, Canada, April 29–May 1, 2008;

[25] Cowherd, J., “Sandblaster 2 Support of See-through Technologies for Particulate Brownout,” MRI Project No 110565.1.001 MRI-PN-110565.1.001, Midwest Research Institute, October 2007;

[26] Bagnold, R. A., The Physics of Blown Sand and Desert Dunes, Dover Publications, Inc., Mineola, NY, 1941;

[27] Owen, P.R., “Saltation of Uniform Grains in Air,” Journal of Fluid Mechanics, Vol. 20 (2), 1964, pp. 225-242;

[28] Milluzzo, J., Sydney, A., Leishman, J. G., In Ground Effect Aerodynamics of Rotors with Different Blade Tips, 66th Annual Forum of the American Helicopter Society, Phoenix, AZ, May 10–13, 2010.

[29] Greeley, R., and J. D. Iversen, Wind as a Geological Process on Earth, Mars, Venus and Titan, Cambridge Univ. Press, New York, 1985;

[30] Shao Y., and Lu, H., “A Simple Expression for Wind Erosion Threshold Friction Velocity,” Journal of Geophysical Research, Vol. 105, (D17), 2000, pp. 22,437–22,443;

[31] Teunissen, H.W., “Characteristics of the Mean Wind and Turbulence in the Planetary Boundary Layer,” UTIAS Review No. 32, University of Toronto Institute for Aerospace Studies, October 1970;

[32] Wang, P., Zhang, J., Dun, H., Herrmann, H. J., & Huang, N. (2020). Aeolian creep transport: Theory and experiment. Geophysical Research Letters, 47, e2020GL088644. https://doi.org/10.1029/2020GL088644;

[33] Lu, H., Shao, Y., “A New Model for Dust Emission by Saltation Bombardment,” Journal of Geophysical Research, Vol. 104, No. D14, pp. 16,827–16,842, July 27, 1999;

[34] https://en.wikipedia.org/wiki/Box-Muller_transform

Author contact:

Antonio Visingardi a.visingardi@cira.it

10 CLASSIFICATION & COPYRIGHT